The Astrophysical Journal, 689:1–16, 2008 December 10

COSMIC REIONIZATION AND THE 21 cm SIGNAL: COMPARISON BETWEEN AN ANALYTICAL MODEL AND A SIMULATION

Mário G. Santos,[1] Alexandre Amblard,[2] Jonathan Pritchard,[3,4] Hy Trac,[4,5] Renyue Cen,[5] and Asantha Cooray[2]

Received 2007 August 21; accepted 2008 July 20

ABSTRACT

We measure several properties of the reionization process and the corresponding low-frequency 21 cm signal associated with the neutral hydrogen distribution, using a large volume, high-resolution simulation of cosmic reionization. The brightness temperature of the 21 cm signal is derived by postprocessing this numerical simulation with a semianalytical prescription. Our study extends to high redshifts ($z \sim 25$) where, in addition to collisional coupling, our postprocessed simulations take into account the inhomogeneities in the heating of the neutral gas by X-rays and the effect of an inhomogeneous Lyα radiation field. Unlike the well-studied case in which spin temperature is assumed to be significantly greater than the temperature of the cosmic microwave background due to uniform heating of the gas by X-rays, spatial fluctuations in both the Lyα radiation field and X-ray intensity affect predictions related to the brightness temperature at $z > 10$, during the early stages of reionization and gas heating. The statistics of the 21 cm signal from our simulation are then compared to existing analytical models in the literature, and we find that these analytical models provide a reasonably accurate description of the 21 cm power spectrum at $z < 10$. Such an agreement is useful, since analytical models are better suited to quickly explore the full astrophysical and cosmological parameter space relevant for future 21 cm surveys. We find, nevertheless, nonnegligible differences that can be attributed to differences in the inhomogeneous X-ray heating and Lyα coupling at $z > 10$, and, with upcoming interferometric data, these differences in return can provide a way to better understand the astrophysical processes during reionization.

Subject headings: cosmology: theory — diffuse radiation — large-scale structure of universe

Online material: color figures

1. INTRODUCTION

One of the key challenges facing cosmology today is understanding in detail how the density distribution of both dark matter and baryons in the universe evolved from a relatively smooth initial state at early times into the nonlinear structures we observe today. This nonlinear structure formation is directly coupled to the formation first of galaxies and, later on, galaxy clusters. The epoch of reionization (EOR) is a crucial stage in the history of galaxy and structure formation, signaling the birth of the first luminous objects as structures first evolved beyond the well-understood linear regime. Although the process by which the intergalactic medium (IGM) became ionized is quite complex, the current view is that when the first protogalaxies and quasars form, they ionize the surrounding gas creating the H II "bubbles." These regions continue to grow and overlap, so that eventually all of the neutral gas in the IGM becomes ionized (Barkana & Loeb 2001; Fan et al. 2006a).

Current primary constraints on the epoch of reionization come from two main sources: the *Wilkinson Microwave Anisotropy Probe* (*WMAP*) determination of the optical depth to recombination through a late-time signature at large angular scales in the cosmic microwave background (CMB) polarization spectrum (Spergel et al. 2007; Zaldarriaga 1997) and the Lyα forest absorption spectra toward high-redshift quasars (e.g., Fan et al. 2001, 2006b). The latter, termed the Gunn-Peterson effect (Gunn & Peterson 1965), is present toward sight lines to quasars out to $z \sim 6.5$ (Becker et al. 2001; Cen & McDonald 2002), showing that reionization should be ending by this time. (It could also indicate a transition in the Gunn-Peterson optical depth from absorption spectra out to $z \sim 4$ and those out to higher redshifts). However, we note that a small neutral fraction is enough to completely absorb the Lyα quasar flux, so these observations themselves cannot be used to properly establish the reionization history of the universe (Lidz et al. 2006.)

In terms of the *WMAP* data, the large angular scale polarization (Page et al. 2007; Dunkley et al. 2008) yields a Thomson optical depth of $\tau = 0.084 \pm 0.016$, so that reionization should happen at $z \sim 10.8 \pm 1.4$ in the favored ΛCDM cosmological model, assuming instantaneous reionization of the universe (Komatsu et al. 2008; Spergel et al. 2007). The reionization process need not be instantaneous, however, and if it is less abrupt (see e.g., Haiman & Holder 2003), then the universe may have begun to partly reionize at an even earlier epoch. Limited by these two constraints, we know that the reionization process should have lasted for at least 500 million years, although there is very little observational evidence as to how this event actually occurred, allowing for various possibilities including double reionization (Cen 2003; Wyithe & Loeb 2003).

While more precise CMB polarization measurements than with *WMAP* alone at large angular scales can provide more information on the reionization history (Holder et al. 2003; Kaplinghat et al. 2003; Mortonson & Hu 2008), it is now generally accepted that detailed information, including the exact history of the reionization process, will become available with 21 cm signal from the neutral hydrogen distribution during and prior to reionization (Madau et al. 1997; Loeb & Zaldarriaga 2004; Gnedin & Shaver 2004; Furlanetto et al. 2004a; Zaldarriaga et al. 2004; Sethi 2005;

[1] CENTRA, Instituto Superior Técnico, 1049-001 Lisbon, Portugal.
[2] Center for Cosmology, Department of Physics and Astronomy, 4186 Frederick Reines Hall, University of California, Irvine, CA 92697.
[3] California Institute of Technology, Mail Code 130-33, Pasadena, CA 91125.
[4] Harvard-Smithsonian Center for Astrophysics, Mail-Stop 51, 60 Garden Street, Cambridge, MA 02138.
[5] Department of Astrophysical Sciences, Princeton University, Princeton, NJ 08544.

Bharadwaj & Ali 2005; Morales & Hewitt 2004). Given the line emission, with frequency selection for observations, the 21 cm data provide a tomographic view of the reionization process (Santos et al. 2005; Furlanetto et al. 2004b), as well as a probe of the dark ages where no luminous sources are present after recombination at a redshift of 1100 (Loeb & Zaldarriaga 2004).

We note that small angular scale CMB anisotropies also capture some information related to reionization, especially the inhomogeneous or patchy nature of the reionization process (Santos et al. 2003; Aghanim et al. 1996; Knox et al. 1998) and through effects such as the Ostriker-Vishniac effect (Ostriker & Vishniac 1986; Vishniac 1987). The 21 cm background and the CMB provide complimentary information in regard to reionization, since the former is related to the neutral hydrogen distribution while the latter is due to the electron content (Cooray 2004). Unfortunately, at such small angular scales, the CMB anisotropy spectrum is rich, with a variety of effects contributing to the overall signal, including galaxy clusters and gravitational lensing. Therefore, the focus is mainly on 21 cm observations, while additional information from the CMB, such as with a high-resolution version of the EPIC concept mission for the CMBPol (Bock 2008), may help extract some properties of the reionization physics.

Motivated by the existing observational constraints and the possibility of studying reionization through the neutral hydrogen content with the proposed 21 cm experiments, such as the Square Kilometer Array (SKA),[6] the Low Frequency Array (LOFAR),[7] and the Mileura Widefield Array (MWA),[8] a great deal of effort has been made recently to understand the 21 cm signal and its information content (see Furlanetto et al. 2006b for a review). In parallel with developments on the experimental front, our theoretical understanding of reionization has also improved both through numerical simulations and analytical models. Numerical simulations provide a detailed description of related astrophysics at these redshifts from first principles by directly solving the nonlinear physics of gravitational collapse, hydrodynamics, and radiative transfer (Gnedin 2000; Razoumov et al. 2002; Sokasian et al. 2003; Ciardi et al. 2003; Kohler et al. 2007; Iliev et al. 2006; Zahn et al. 2007; McQuinn et al. 2007). However, proper sampling of the epoch of reionization requires simulations with large volumes ($\sim$100 Mpc h^{-1})^3 (Barkana & Loeb 2004; Furlanetto et al. 2004c) and with adequate mass resolution to resolve halos, where first-light sources are expected to form ($M \sim 10^6\ M_\odot\ h^{-1}$). The large volume and the large particle number makes such simulations computationally expensive, especially in the context of hydrodynamical calculations related to the gas physics. The usual approach is to use high-resolution but small-volume simulations or large-volume but low mass resolution simulations. In this paper we make use of a simulation that directly resolves halos below $10^8\ M_\odot$ in a box of 100 Mpc h^{-1}, considered essential to properly take into account the bubble growth during reionization (Shin et al. 2008).

Due to the challenging computational requirements of numerical models, progress on the modeling front has come mostly from analytical descriptions on the volume filling factor and size distribution of ionized regions, as well as the power spectrum of the ionized fraction and density fields (Furlanetto et al. 2004c, 2006a; Sethi 2005; Barkana 2007). These analytical descriptions have been quite useful for understanding the possible contributions to the 21 cm signal at high redshifts (Barkana & Loeb 2005; Pritchard & Furlanetto 2007) or under certain simplified conditions, such as the case in which spin temperature of neutral gas is significantly higher than that of the CMB. The analytical approach is also crucial for exploring the extent to which the full parameter space of the 21 cm signal and associated cosmology can be established with data from future surveys planned with MWA, LOFAR, and SKA (Santos & Cooray 2006; McQuinn et al. 2006; Mao et al. 2008).

An intermediate approach, based on semianalytical models combined with seminumerical models, has also been developed (Zahn et al. 2007; Mesinger & Furlanetto 2007). It relies on the generation of realizations of halo distributions directly from the linear density field and implementing the corresponding ionization map using criteria similar to the analytical models. These make it possible to preserve the spatial information of the reionization process as provided by simulations, while achieving a much larger dynamic range than that provided by radiative transfer codes.

In the future, once data become available with the first-generation low-frequency radio interferometers, it will be useful to have fast techniques to extract the parameters from the measurements, such as the power spectrum 21 cm brightness temperature. While detailed numerical simulations to seminumerical models can be considered for this purpose, it is unlikely that such simulations can be carried out for all variations in parameters of interest, which include both astrophysical and cosmological quantities. In this sense, it is more useful to make use of analytical methods supplemented by well-motivated fitting functions for quantities such as the power spectrum of the ionization fraction during reionization in terms of the power spectrum of density perturbations, which depends on cosmological parameters. This is the approach taken in predictions related to 21 cm cosmological information content (Santos & Cooray 2006; Mao et al. 2008), but we still need to improve our approximations in such an approach by continuing to study first-principle numerical models of reionization and 21 cm physics to test assumptions on the existing analytical models.

Due to time constraints associated with numerical models, it is very likely that analytical models are the preferred choice for intensive astrophysical and cosmological parameter studies from the 21 cm signal observed with low-frequency radio interferometers. In the case of cosmological parameter estimation with CMB or from galaxy clustering, the numerical computations provide solutions to an analytical derivation of either the CMB signal or the dark matter clustering power spectrum. Unfortunately, for the 21 cm anisotropies, such an approach is likely to be complicated, especially during reionization, although at very high redshifts ($\sim$50), where the physics is simple, a quick numerical calculation can be carried out from first principles (Lewis & Challinor 2007).

In this paper we determine several properties of reionization using a state-of-the-art large-volume and high-resolution simulation of cosmic reionization based on a photon-advection radiative transfer scheme combined with a dark matter N-body simulation with recipes for baryons and star formation (Shin et al. 2008). While the simulation itself is of dark matter, the postprocessing allows us to convert the star formation rate predicted in the simulation to the spin temperature of the gas in the simulation. Furthermore, we determine the 21 cm brightness temperature up to $z \sim 25$, by postprocessing the simulation output with a semianalytical prescription for the X-ray heating of the gas, the Lyα coupling, and the collisional coupling, and by taking fully into account the spatial fluctuations in these quantities. The existing simulations of the reionization and predictions related to 21 cm signal from such simulations generally ignore the spatial inhomogeneities associated with X-ray heating and the Lyα radiation field, although anisotropies of the 21 cm brightness temperature

[6] At http://www.skatelescope.org.
[7] At http://www.lofar.org.
[8] At http://www.haystack.mit.edu/arrays/mwa.

are expected to be sourced by such inhomogeneities at high redshifts. We compare results based on simulations with estimates from a fast analytical model of reionization (Furlanetto et al. 2004c; McQuinn et al. 2005; Lidz et al. 2007).

Throughout the paper we use of the following cosmological parameters: $\Omega_m = 0.26$, $\Omega_\Lambda = 0.74$, $\Omega_b = 0.044$, $h = 0.72$, and $n_s = 0.96$ and $\sigma_8 = 0.77$ based on the results from *WMAP*, SDSS, *HST*, and SN data (see Spergel et al. 2007 and references therein). The optical depth is $\tau \approx 0.09$, consistent with the WMAP-5 result. The paper is organized as follows: In the next section, we outline details related to the reionization process and compare results from the simulation and the analytical calculation. We then proceed to describe how to calculate the corresponding 21 cm signal in § 3 with details of the simulation in § 4. Again we show a comparison of the results from simulation to analytical models (§ 5). We conclude with a summary of our results in § 6.

2. COSMIC REIONIZATION

2.1. *Numerical Simulation*

In this paper we make use of one of the largest simulations of cosmic reionization that has been completed to date (Shin et al. 2008). We refer the reader to Shin et al. (2008) for details related to the hybrid code that contains a N-body algorithm for dark matter, prescriptions for baryons and star formation, and a radiative transfer (RT) algorithm for ionizing photons. We provide a basic summary of the simulation parameters here as necessary for this study.

The hybrid simulation involves a high-resolution N-body calculation of 2880^2 dark matter particles in a $L = 100$ Mpc h^{-1} box. With a particle mass resolution of $3.02 \times 10^6\ M_\odot\ h^{-1}$, halos can be reliably resolved down to masses of $\sim 10^8\ M_\odot\ h^{-1}$, accounting for the majority of photoionizing sources. The simulation distinguishes between the first generation, Population III (Pop III) stars and the second generation, Population II (Pop II) stars by following the chemical enrichment of the ISM and IGM as described in Trac & Cen (2007). The input UV spectrum is divided in three energy ranges 13.61 eV $< h\nu \leq$ 24.59 eV, 24.59 eV $< h\nu \leq$ 54.42 eV, and $h\nu >$ 54.42 eV, with Pop II stars with a Salpeter IMF providing 1100, 3830, and 270 ionizing photons per baryon of star formation, respectively. For Pop III stars with a top-heavy IMF, the corresponding numbers are 15,000, 51,500, and 3500 (Schaerer 2002, 2003). The radiative transfer of ionizing photons is calculated simultaneously as dark matter evolves with the N-body code and with star formation and baryon physics evolving according to recipes each step of the way. In this way, our simulation differs from other descriptions in the literature in which radiative transfer and baryon physics are obtained by post-processing a completed N-body run.

Note that we do not use the halo model of Trac & Cen (2007) for prescribing baryons and star formation. Instead, an alternative approach is taken in which we calculate the local matter density ρ and velocity dispersion σ_v for each particle. The baryons are assumed to trace the dark matter distribution on all scales, and we obtain the local baryon density $\rho_b = \rho(\Omega_b/\Omega_m)$ and gas temperature $T = \mu\sigma_v 2/(3k)$. Star formation is only allowed to occur in particles with densities $\rho > 100\rho_{\rm crit}(z)$ and temperatures $T > 10^4$ K, thus restricting star formation to regions within the virial radius of larger halos, and these halos are fully resolved given the low-mass resolution of our simulation.

The radiative transfer of ionizing radiation uses a photon-advection scheme and was run simultaneously with the N-body calculations using a RT grid with 360^3 cells. However, the ionization and recombination calculations were done for each particle individually rather than on the grid to preserve small-scale information down to scales of several comoving kpc h^{-1}. For post-processing, the dark matter, baryons, and radiation are collected on a grid with 720^3 cells and the data are saved every 10 million years from $z = 25$ down to $z = 5$.

We start our analysis of the reionization process by examining a sequence of cuts through the simulation box of the fraction of free electrons x_i (the ionization fraction), shown in Figure 1. In this simulation box, reionization begins at a redshift of $\sim$18. The ionized bubbles have complex shapes and cannot be simply described with spherical models for the three-dimensional H II regions surrounding UV sources. Complete overlap of the ionization patches occurs at the redshift of $z \sim 6$. Note that although the ionization fraction can have a range of values between 0 and 1, most of the volume in the simulation is almost completely ionized (very high x_i) or completely neutral, thus favoring the current view of reionization based on the percolation of large ionized bubbles. Figure 2 shows the evolution of the average ionization fraction compared with the values if we assume that gas is completely ionized inside bubbles ($x_i = 1$) and completely neutral outside ($x_i = 0$). Bubbles are defined by the threshold $x_i > 0.5$.

2.2. *Analytical Models*

Our analytic model for reionization, which we compare with results from our numerical simulation, follows the approach of Furlanetto et al. (2004c). The mass of the ionized gas is linked to the mass in galaxies by the *Ansatz*, $m_{\rm ion} = \zeta m_{\rm gal}$, where ζ is an ionizing efficiency. A spherical region of gas of mass m is considered ionized if it contains sufficient sources to self-ionize, i.e., $f_{\rm coll} \geq \zeta^{-1}$. In the excursion set formalism this criteria is well described by a mass dependent linear barrier $B(m,\ z) = B_0 + B_1\sigma^2(m)$, where $\sigma^2(m)$ is the variance of the density fluctuations on the scale m. With this we can calculate the mass function of bubbles (the comoving number density of H II regions with masses in the range $m \pm dm/2$):

$$\frac{dn(m)}{dm}dm = \sqrt{\frac{2}{\pi}}\frac{\bar{\rho}}{m^2}\left|\frac{d\log\sigma}{d\log m}\right|\frac{B_0}{\sigma(m)}\exp\left[-\frac{B^2(m,\ z)}{2\sigma^2(m)}\right]dm, \tag{1}$$

where $\bar{\rho}$ is the mean mass density of the universe.

Note that we renormalize the resulting mass function to enforce the requirement $\bar{Q} = \zeta f_{\rm coll}$, where $\bar{Q}$ is the filling fraction of bubbles. Next we must determine the appropriate value for the ionization efficiency ζ. We allow ζ to vary with redshift and require that $x_i = \zeta f_{\rm coll}$ at all redshifts. Here x_i is determined from the simulations, so that we bypass the need for a source prescription when defining ζ, and we assume a Press-Schechter mass function when determining $f_{\rm coll}$. In principle, using the Sheth-Tormen mass function gives a weaker redshift dependence for ζ, but we use Press-Schechter for greater consistency with the reionization model of Furlanetto et al. (2004c).

To calculate fluctuations in the 21 cm brightness temperature, we first need to calculate the correlation functions in the ionization fraction $\xi_{x_i x_i}$, density $\xi_{\delta\delta}$, and the cross-correlation of these two quantities $\xi_{x_i\delta}$, where

$$\xi_{ab} \equiv \left\langle (a - \bar{a})\left(b - \bar{b}\right)\right\rangle \tag{2}$$

and $\delta = \rho/\bar{\rho} - 1$. We use the halo model to calculate $\xi_{\delta\delta}$ (Cooray & Sheth 2002). Furlanetto et al. (2004c) present an ad hoc model for the correlation functions ξ_{xx} and $\xi_{x\delta}$, designed to ensure that the correct limiting behavior as $x_H \rightarrow 0,\ 1$ is obeyed. A fundamental problem with their approach is that bubbles are assumed to be spherical at all times, leading to problems describing the

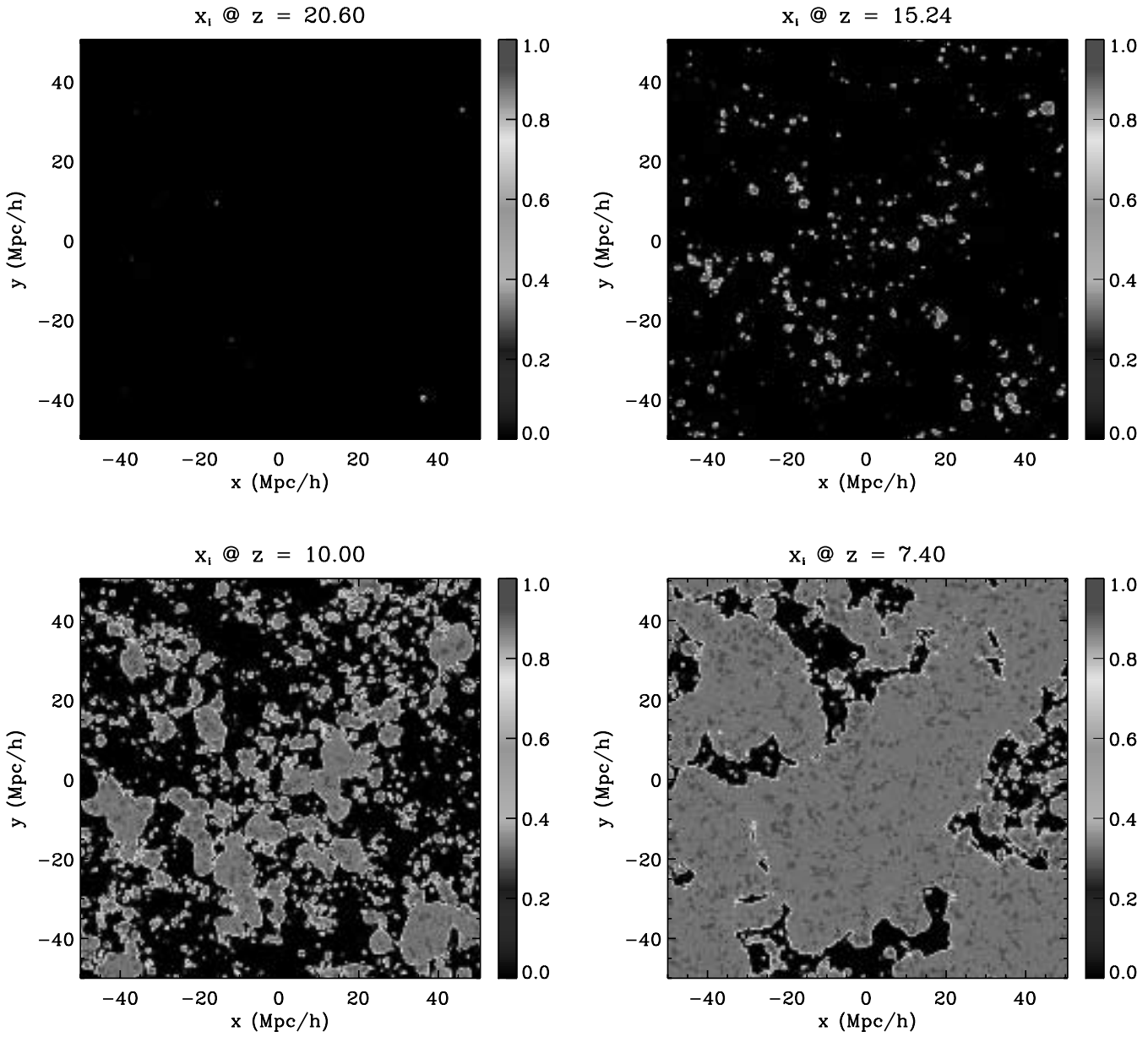

FIG. 1.—Maps of the ionization fraction from the simulation at redshifts $z = 20.60$, 15.24, 10.00, and 7.40, corresponding to $\bar{x}_i = 0.0002$, 0.03, 0.35, and 0.84. Note how there is a clear separation between the highly ionized regions (*in gray*) and the mostly neutral IGM (*black*). [*See the electronic edition of the Journal for a color version of this figure.*]

overlap of bubbles properly. McQuinn et al. (2005) later attempted to modify the Furlanetto et al. (2004c) model to forbid bubble overlap. However, since neither of these models correctly handles bubble overlap, we choose to use the original formulation of Furlanetto et al. (2004c). However, we incorporate the corrected calculation of the bubble bias, as noted by McQuinn et al. (2005). We note that a more physically motivated method based on the two-step approximation has recently been developed by Barkana (2007). Given the availability of simulations, however, and for purposes of the present discussion, where we are investigating the extent to which a simple model for parameter estimates can be compared to numerical simulations and is found in general to provide good agreement, such details are unnecessary.

The three-dimensional power spectra of our simulation were performed using the fast Fourier transform package fftw-3.1.1[9] and is defined through $\langle a(\bar{k})b^*(\bar{k}')\rangle \equiv (2\pi)^3\delta^3(\bar{k}-\bar{k}')P_{ab}(k)$. We then binned our modes with $\delta k = 2\pi/100(\mathrm{Mpc}\ h^{-1})^{-1}$ and computed the average power spectra in each bin. Throughout the paper we plot the dimensionless power spectrum, $\Delta^2 = k^3P(k)/2\pi^2$, which gives the contribution to the variance per logarithmic interval in k. In order to test the analytical calculation, we show in Figure 3 the ratio of the three-dimensional power spectrum of the ionization fraction to the matter density for the simulation and analytical models.

The features in the power spectrum of ionization fraction relative to density perturbations can be described as follows. At scales much larger than the bubble size, the ionization fraction power spectrum is proportional to the matter density with an overall scaling that can be assigned to the bias factor of the ionized regions. From the simulation results represented by the dotted lines this can be seen more easily at high redshifts where bubble sizes are small. At these redshifts ($z = 20.60$ and 15.24), there is an increase in the ionization power spectrum at small scales due to

[9] See http://www.fftw.org.

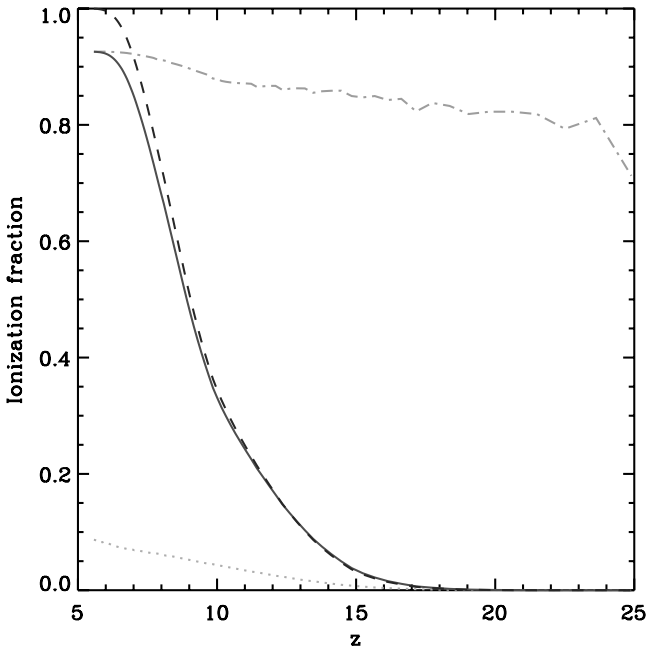

FIG. 2.—Average ionization fraction as a function of redshift from the simulation (*solid line*) and assuming complete ionization of the bubbles (*dashed line*), defined for $x_i > 0.5$. The dot-dashed line shows the ionized fraction inside the bubbles, while the dotted line shows the ionized fraction in the IGM (defined has $x_i < 0.5$). [*See the electronic edition of the Journal for a color version of this figure.*]

the Poisson behavior of the bubble distribution. This is analogous to the shot-noise component of the galaxy power spectrum even at low redshifts that dominate fluctuations at nonlinear scales.

As we move to lower redshifts and larger bubbles, Figure 3 shows more clearly that the power spectrum of the ionization fraction $P_{x_i x_i}$ decreases on physical scales smaller than the typical bubble size, due to the smoothing effect of bubbles. Note, however, that the decrease is not abrupt, since there is a distribution of bubble sizes at any redshift with varying ionization fractions. The analytical calculation we discussed so far (*dashed line*) seems to agree reasonably well with the simulation, although at larger ionization fractions ($x_i > 0.8$), when the bubbles occupy most of the simulation volume, there are some differences. This difference is probably due to the finite size of the simulation box, which effectively limits the bubble size and reduces power on large scales. Note, however, that even if our simulations involved larger volumes, the power could continue to be smaller than in the analytical case, since the simulation accounts for self-shielding of dense regions that remain neutral. This causes the bubble growth to stall and in return limit the maximum bubble size (Furlanetto & Oh 2005).

In Figure 3, in addition to the comparison between results from our numerical simulation and a widely used analytical model, we also compare our results with two simple fitting functions of the ionization fraction given the density field power spectrum. We do this comparison, since in exploring the full parameter space probed by 21 cm experiments (Santos & Cooray 2006; Mao et al. 2008), fitting formulae are used in calculations to describe the power spectrum of the ionization fraction without relying on detailed analytical models or numerical calculations of bubble growth. Here we compare our results to two fitting functions in the literature where the power spectrum of the ionized fraction $P_{x_i x_i}$ is given as

$$P_{x_i x_i}(k) = b_{x_i x_i}^2 e^{-\left(kR_{x_i x_i}\right)^2} P_{\delta\delta}(k), \quad (3)$$

$$P_{x_i x_i}(k) = b_{x_i x_i}^2 \left[1 + \alpha_{x_i x_i}(kR_{x_i x_i}) + (kR_{x_i x_i})^2\right]^{-\gamma/2} P_{\delta\delta}(k), \quad (4)$$

where the first approximation is from Santos & Cooray (2006) and the second is from Mao et al. (2008) and $b_{x_i x_i}$, $\alpha_{x_i x_i}$, γ, and $R_{x_i x_i}$ are free parameters that are varied to obtain a fit to the simulation results. In Table 1 we list the values that were obtained by comparing numerical simulations with the above form.

While these two fitting functions have been used in the literature when making predictions related to how well cosmological parameters can be measured with 21 cm interferometers such as MWA and LOFAR, as can be seen from Figure 3, neither of these functions are completely accurate descriptions of the power spectrum of ionized fraction over all the redshift range we have studied with simulations. This is due to the fact that, for example, the first approximation from Santos & Cooray (2006) assumes that bubbles can be described with a single size leading to a sharp cutoff at the wavenumber corresponding to the inverse radius, while from simulations and in the analytical model of Furlanetto et al. (2004c) the bubbles have varying sizes. At $z < 15$, when bubbles have started to grow, the fitting formula of Mao et al. (2008) provides an improved fit given the additional freedom provided by the parameters α and γ, and this description is probably adequate for now for purposes of predicting the extent to which cosmological parameters can be measured with a 21 cm experiment. On the other hand, when real data are being model-fitted real data, it may be necessary to improve the estimate of $P_{x_i x_i}(k)$ beyond simple fitting functions such as the ones listed in equations (3) and (4). In this respect, we note that the analytical model of Furlanetto et al. (2004c) provides a more accurate description of the results from our numerical simulation and a clearer interpretation of the values obtained. If such a model can be further improved to quickly explore a large parameter space in a reasonable time, it may be useful to implement it in a numerical code for parameter estimates, such as one based on the Markov chain Monte Carlo technique, instead of simply using fitting functions to estimate parameter values from 21 cm interferometers.

Figure 4 (*left*) shows the cross-power spectrum between the ionization fraction and the density field. The peak of this cross-power spectrum moves to larger scales as the redshift decreases, since it is related to the typical size of bubbles during reionization. At smaller scales, there is some indication that the cross-correlation power spectrum becomes negative in the numerical simulation, suggesting more of an anticorrelation than what is seen in the analytical model. We believe this is partly due to small neutral regions inside H II bubbles because the simulation takes into account the self-shielding of dense regions. Note, however, that as reionization progresses and the radiation intensity becomes larger, the existence of small fingers from large bubbles protruding into the now small neutral regions will play an important part in this anticorrelation.

Similar to equation (4), we can also write the cross-power spectrum between x_i and δ assuming a perfect correlation of the two fields, such that

$$P_{x_i\delta} = \sqrt{P_{x_i x_i} P_{\delta\delta}}. \quad (5)$$

and by making use of the fitting formulae for the ionization fraction power spectrum from equation (3), as used by Santos & Cooray (2006). In Mao et al. (2008) this cross-power spectrum is modeled as $P_{x_i\delta} = b_{x_i\delta}^2 \exp[-\alpha_{x_i\delta}(kR_{x_i\delta}) - (kR_{x_i\delta})^2] P_{\delta\delta}$, and in Figure 4 (*right*) we also show this case with a new set of parameters ($b_{x_i\delta}$, $\alpha_{x_i\delta}$, $R_{x_i\delta}$). Here we plot the correlation coefficient $r = P_{x_i\delta}/(P_{x_i x_i} P_{\delta\delta})^{1/2}$, and we compare the fitting function motivated by Mao et al. (2008) to numerical simulations. While there is a good overall agreement between the simulations and the analytical model, we find differences at $z \sim 20$ between the two

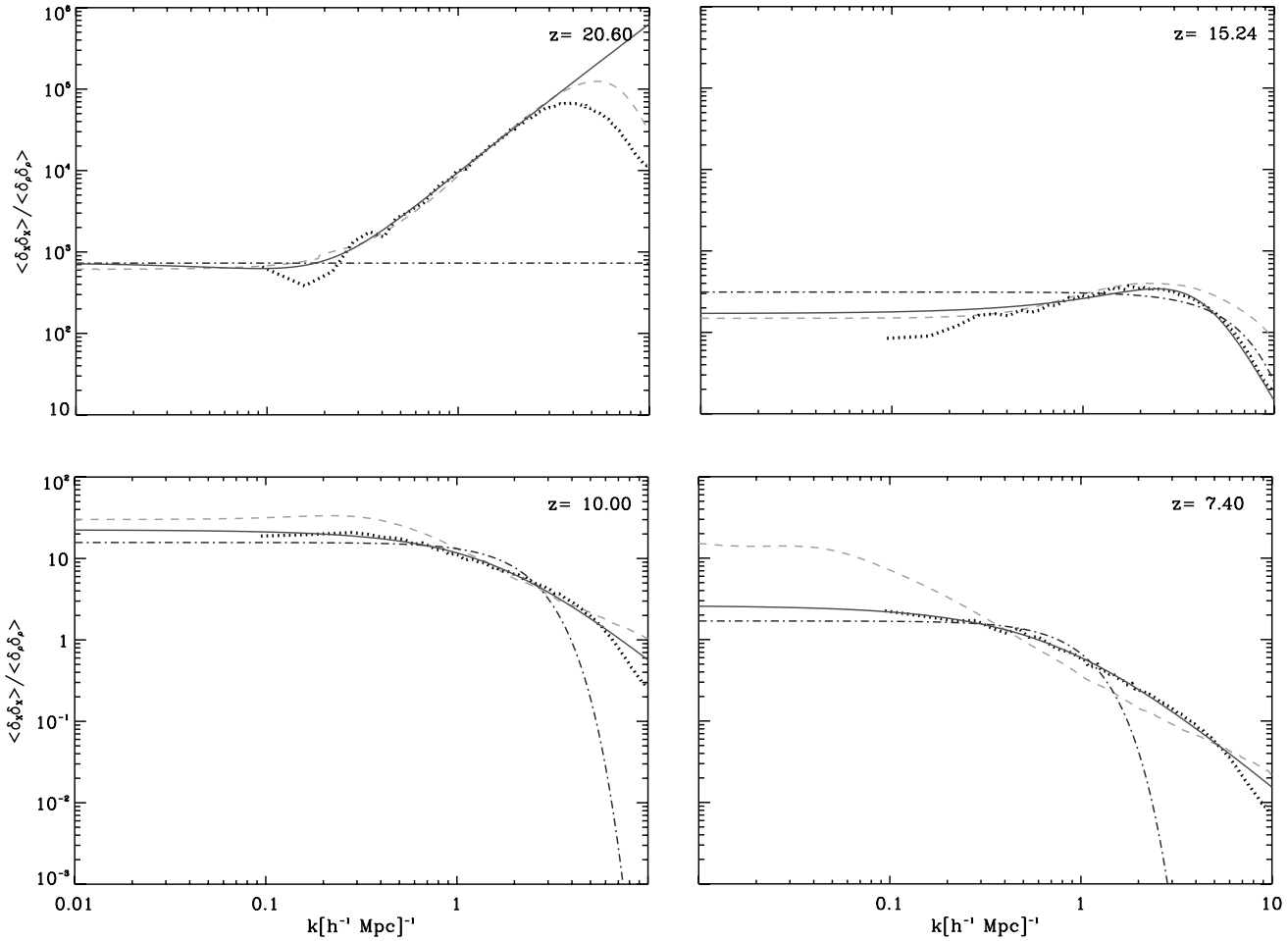

FIG. 3.—Ratio of the power spectra of the ionization fraction, $\delta_{x_i} \equiv x_i/\bar{x}_i - 1$ to the matter one, $\delta \equiv \rho/\bar{\rho} - 1$. The simulation corresponds to the dotted line, while the dashed line gives the results of the analytical model followed in the paper (based on Furlanetto et al. 2004c). Lines fit curves using the two-parameter model suggested in Santos & Cooray (2006), while solid curves use the model in Mao et al. (2008). Redshifts, as labeled from top-left to bottom-right are $z = 20.6$, 15.2, 10.0, and 7.4, corresponding to $\bar{x}_i = 0.0002$, 0.03, 0.35, and 0.84, respectively. [*See the electronic edition of the Journal for a color version of this figure.*]

descriptions. Such a disagreement, however, is not a concern for first-generation 21 cm observations, since the instruments involved mostly concentrate on $z \sim 6$ to 9 during reionization.

3. THE 21 cm SIGNAL: THEORY

We present here the overall calculation of the 21 cm signal. Details specific to the simulation and the analytical calculation considered in this paper will be given later in the appropriate sections.

3.1. *Brightness Temperature*

One of the best ways to observe the reionization process is through the 21 cm brightness temperature, corresponding to the change in the intensity of the CMB radiation due to absorption or emission when it travels through a patch of neutral hydrogen. It is given, at an observed frequency ν in the direction $\hat{n}$, by

$$\delta T_b(\hat{n},\ \nu) \approx \frac{T_S - T_\gamma}{1+z}\tau, \tag{6}$$

TABLE 1
PARAMETERS OF THE IONIZATION FRACTION POWER SPECTRUM MODEL

Function	Parameter	$z = 20.6$	$z = 15.2$	$z = 10.0$	$z = 7.4$
Eq. (3)	$R_{x_i x_i}$ (h^{-1} Mpc)	0	0.16	0.42	0.96
	$b_{x_i x_i}$	27	17.7	4.0	1.3
Eq. (4)	$R_{x_i x_i}$ (h^{-1} Mpc)	−4.53	0.23	0.62	1.24
	$\alpha_{x_i x_i}$	0.83	−1.12	0.93	1.48
	γ	−1.77	3.72	1.93	1.99
	$b_{x_i x_i}$	27.2	13.1	4.7	1.6

NOTES.—As described in eqs. (3) and (4) fitted to our simulation power spectrum measured at $z = 20.6$, 15.2, 10, and 7.4. Note that to get the "physical" $R_{x_i x_i}$ based on our definitions one should multiply the above values by a factor of (2π).

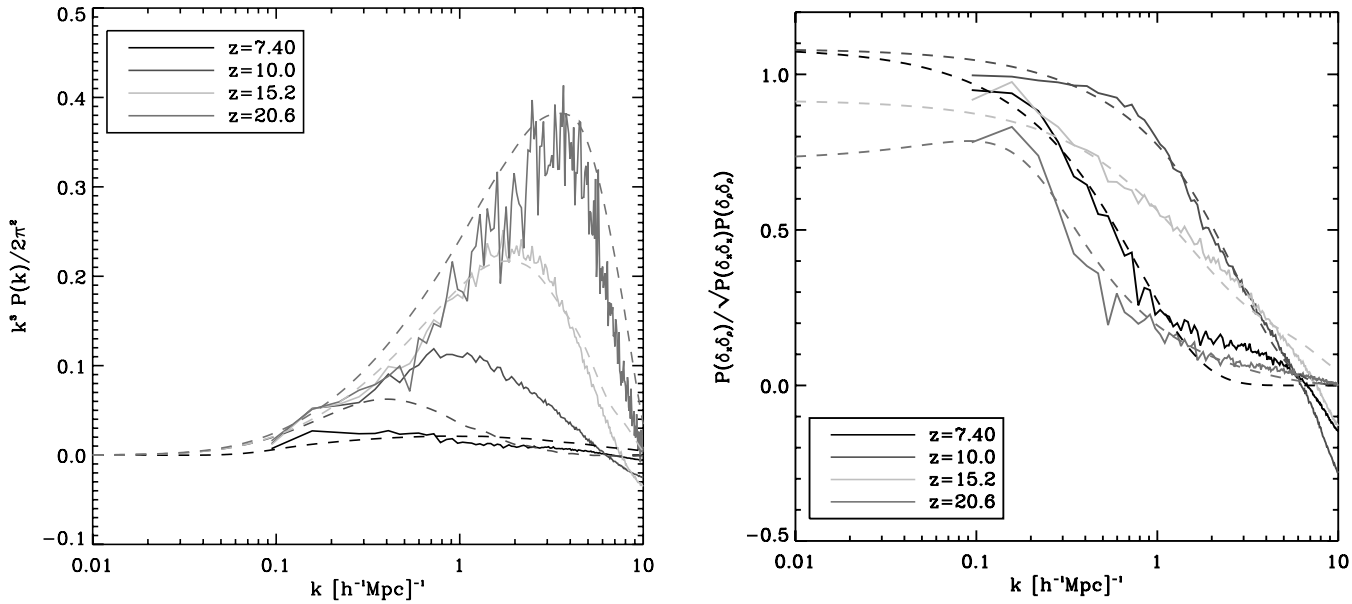

FIG. 4.—*Left*: Cross-power spectra of the ionization fraction and matter density $\langle \delta_{x_i} \delta \rangle$ from simulations. The solid lines give the simulation values, while dashed lines are for the analytical model from Furlanetto et al. From top to bottom the curves correspond to $z = 20.6$, 15.2, 10.0, and 7.4. *Right*: Correlation coefficient, $r = P_{x_i\delta}/(P_{x_i x_i} P_{\delta\delta})^{1/2}$, with simulations (*solid line*) and the fitting function of Mao et al. (2008) (*dashed line*) for the same redshifts as the left panel. [*See the electronic edition of the Journal for a color version of this figure.*]

where T_S is the temperature of the source (the spin temperature of the IGM), z is the redshift corresponding to the frequency of observation ($1 + z = \nu_{21}/\nu$, with $\nu_{21} = 1420$ MHz), and $T_\gamma = 2.73(1 + z)K$ is the CMB temperature at redshift z. The optical depth, τ, of this patch in the hyperfine transition (Field 1959) is given in the limit of $k_B T_s \gg h\nu_{21}$ by

$$\tau = \frac{3c^3 \hbar A_{10} n_{\rm H\,I}}{16 k \nu_{21}^2 T_S (1+z)(\partial V_r/\partial r)}, \tag{7}$$

where A_{10} is the spontaneous emission coefficient for the transition (2.85×10^{-15} s^{-1}), $n_{\rm H\,I}$ is the neutral hydrogen number density, and $\partial V_r/\partial r$ is the gradient of the total radial velocity along the line of sight (with $V_r \equiv \boldsymbol{V} \cdot \hat{\boldsymbol{n}}$); on average $\partial V_r/\partial r = H(z)/(1 + z)$. In this paper we neglect perturbations from the peculiar velocity of the gas. The neutral density can be expressed as $n_{\rm H\,I} = f_{\rm H\,I} X \rho_b / m_p$ where $f_{\rm H\,I} = \rho_{\rm H\,I}/\rho_{\rm H}$ is the fraction of neutral hydrogen (mass weighted), $X \approx 0.76$ is the hydrogen mass fraction, ρ_b is the baryon density, and m_p the proton mass. The 21 cm temperature is then

$$\delta T_b(\hat{\boldsymbol{n}},\ \nu) \approx 23 f_{\rm H\,I} \frac{\rho_b}{\bar{\rho}_b} \left(1 - \frac{T_\gamma}{T_S}\right) \left(\frac{h}{0.7}\right)^{-1} \times \left(\frac{\Omega_b h^2}{0.02}\right) \left[\left(\frac{0.15}{\Omega_m h^2}\right)\left(\frac{1+z}{10}\right)\right]^{1/2} \text{mK}. \tag{8}$$

In order to proceed, we need a prescription to calculate the spin temperature of the gas.

3.2. *Spin Temperature*

The spin temperature is coupled to the hydrogen gas temperature (T_K) through the spin-flip transition, which can be excited by collisions or by the absorption of Lyα photons (the Wouthusysen-Field effect), and we can write

$$1 - \frac{T_\gamma}{T_S} = \frac{y_{\rm tot}}{1 + y_{\rm tot}} \left(1 - \frac{T_\gamma}{T_K}\right), \tag{9}$$

where $y_{\rm tot} = y_\alpha + y_c$ is the sum of the radiative and collisional coupling parameters and we are already assuming that the color temperature of the Lyα radiation field at the Lyα frequency is equal to T_K. When the coupling to the gas temperature is negligible (e.g., $y_{\rm tot} \sim 0$), $T_S \sim T_\gamma$ and there is no signal. On the other hand, for large $y_{\rm tot}$, T_S simply follows T_K.

Collisions can be important for decoupling the H I 21 cm spin temperature from the CMB, especially at high redshifts (Nusser 2005), and the coupling coefficient is given by

$$y_c = \frac{4 T_\star}{3 A_{10} T_\gamma} \left[\kappa_{1-0}^{\rm HH}(T_k) n_{\rm H} + \kappa_{1-0}^{e{\rm H}}(T_k) n_e\right], \tag{10}$$

where $T_\star \equiv hc/k\lambda_{21\,\rm cm} = 0.0628$ K, $\kappa_{1-0}^{\rm HH}$ is tabulated as a function of T_k (Allison & Dalgarno 1969; Zygelman 2005), $\kappa_{1-0}^{e{\rm H}}$ is taken from Furlanetto & Furlanetto (2007) and n_e is the electron number density (see also Kuhlen et al. 2006). For a more detailed analysis of the collisional coupling, see Hirata & Sigurdson (2007).

The Wouthuysen-Field effect (Wouthuysen 1952; Field 1959) coupling is given by

$$y_\alpha = \frac{S_\alpha J_\alpha}{J_c}, \tag{11}$$

with

$$J_c \equiv \frac{16\pi^2 T_\star e^2 f_\alpha}{27 A_{10} T_\gamma m_e c} \approx 5.552 \times 10^{-8}(1+z)\ \text{m}^{-2}\ \text{s}^{-1}\ \text{Hz}^{-1}\ \text{sr}^{-1}, \tag{12}$$

where $f_\alpha = 0.4162$ is the oscillator strength of the Lyα transition and $(1 + z)$ comes from T_γ. In equation (11) S_α is a correction factor of order unity, which describes the detailed structure of the photon distribution in the neighborhood of the Lyα resonance (Chen & Miralda-Escudé 2004; Hirata 2006; Chuzhoy & Shapiro 2007; Furlanetto & Pritchard 2006). We use the approximation for S_α outlined in Furlanetto et al. (2006b). The proper Lyα photon intensity, J_α (the spherical average of the number of photons hitting

a gas element per unit proper area per unit time per unit frequency per steradian) is given by a sum over the hydrogen levels n,

$$J_\alpha(\boldsymbol{x},\ z) = \frac{(1+z)^2}{4\pi}\sum_{n=2}^{n_{\max}} f_{\rm rec}(n) \times \int \frac{d\Omega'}{4\pi}\int_0^{x_{\max}(n)} dx'\epsilon_\alpha\left(\boldsymbol{x}+\boldsymbol{x}',\ \nu_n',\ z'\right), \quad (13)$$

where $f_{\rm rec}(n)$ is the fraction of Lyman-n photons that cascade through Lyα and $\epsilon(\boldsymbol{x},\ \nu_n,\ z)$ is the comoving photon emissivity, defined as the number of photons emitted at position $\boldsymbol{x}$, redshift z and frequency ν per comoving volume per proper time and frequency. Note that the redshift z' in equation (13) is such that $x' = \int_z^{z'} cH^{-1}\,dz''$. The absorption at level n at redshift z corresponds to an emitted frequency at z' of

$$\nu_n' = \nu_{\rm LL}\left(1-n^{-2}\right)\frac{(1+z')}{(1+z)}, \quad (14)$$

in terms of the Lyman limit frequency $\nu_{\rm LL}$, and $x_{\max}(n)$ corresponds to the comoving distance between z and $z_{\max}(n)$ given by

$$1+z_{\max}(n) = (1+z)\frac{\left[1-(n+1)^{-2}\right]}{(1-n^{-2})}. \quad (15)$$

If the photon emissivity, ϵ, is homogeneous, equation (13) can be written as (Barkana & Loeb 2005)

$$J_\alpha(z) = \frac{(1+z)^2}{4\pi}\sum_{n=2}^{n_{\max}} f_{\rm rec}(n)\int_z^{z_{\max}(n)}\frac{c\,dz'}{H(z')}\epsilon_\alpha\left(\nu_n',\ z'\right). \quad (16)$$

3.3. *Gas Temperature*

Once star formation has gotten underway, a population of stellar remnants will be produced capable of generating highly energetic X-rays. Several candidate X-ray sources exist, including X-ray binaries in starburst galaxies, inverse Compton scattering of CMB photons from relativistic electrons in supernova remnants (SNRs; Oh et al. 2003), and miniquasars. X-rays may contribute to reionization, although constraints from the unresolved soft X-ray background suggest that this is not the dominant source of ionizing photons (Dijkstra et al. 2004). More importantly, as X-rays ionize hydrogen they deposit much of their energy as heat. This X-ray preheating can easily be sufficient to heat the IGM above the temperature of the CMB. Although hard X-rays have a mean free path comparable to the Hubble size, most of the heating turns out to be done by soft X-rays ($E \lesssim 2$ keV), which can produce significantly inhomogeneous heating at high redshifts (Pritchard & Furlanetto 2007).

We calculate the X-ray heating following the model of Furlanetto (2006). We model X-ray sources with a spectral distribution function (number of photons per unit comoving volume per unit time and frequency) that is a power law with index α_S:

$$\hat{\epsilon}_{\rm X}(\nu) = \frac{L_0}{h\nu_0}\left(\frac{\nu}{\nu_0}\right)^{-\alpha_S-1}, \quad (17)$$

and the pivot energy is $h\nu_0 = 1$ keV. We assume emission within the band 0.1–30 keV and set the normalization constant L_0 by requiring the integrated power density $P = \int d\nu L_0(\nu/\nu_0)^{-\alpha_S}$ to be $3.4\times10^{40} f_{\rm X}$ ergs s^{-1} Mpc^{-3} when integrated between 0.1 and 30 keV, but with a highly uncertain constant factor $f_{\rm X}$. This normalization is chosen so that, with $f_{\rm X} = 1$, the total X-ray luminosity per unit SFRD (star formation rate density) is consistent with that observed in starburst galaxies in the present epoch (see Furlanetto 2006 for further details). Typical values are $\alpha_S = 1.5$ for starbursts, $\alpha_S = 1.0$ for supernovae remnants, and $\alpha_S = 0.5$ for the X-ray background generated by miniquasars. These spectral indices are consistent with measured spectra of known X-ray sources, although it is largely uncertain whether low-redshift sources can be fully considered as a representation of source spectra at high redshifts.

We link the total X-ray emissivity (number of photons per SFRD per unit comoving volume per unit frequency and time) to the star formation rate by

$$\hat{\epsilon}_{\rm X}(\boldsymbol{x},\ z,\ \nu) = \hat{\epsilon}_{\rm X}(\nu)\left[\frac{\rm SFRD(\boldsymbol{x},\ z)}{M_\odot\ {\rm yr}^{-1}\ {\rm Mpc}^{-3}}\right]. \quad (18)$$

The X-ray number flux per unit frequency is then

$$J_{\rm X}(\boldsymbol{x},\ z,\ \nu) = \int d^3x'\frac{(1+z)^2}{4\pi|\boldsymbol{x}'|^2}\hat{\epsilon}_{\rm X}\left(\boldsymbol{x}+\boldsymbol{x}',\ \nu_n',\ z'\right)e^{-\tau(z,\nu,\boldsymbol{x},\boldsymbol{x}')}, \quad (19)$$

where again $|\boldsymbol{x}'|$ is the comoving distance between z and z', and ν' is the emission frequency at z' corresponding to an X-ray frequency ν at z

$$\nu' = \nu\frac{(1+z')}{(1+z)}. \quad (20)$$

The optical depth is given by

$$\tau(z,\ \nu,\ \boldsymbol{x},\ \boldsymbol{x}') = \int dl[n_{\rm H\,I}\sigma_{\rm H\,I}(\nu'') + n_{\rm He\,I}\sigma_{\rm He\,I}(\nu'') + n_{\rm He\,II}\sigma_{\rm He\,II}(\nu'')], \quad (21)$$

where the integral is along the photon path in proper units between emission ($\boldsymbol{x}+\boldsymbol{x}'$) at redshift z' and reception ($\boldsymbol{x}$) at redshift z, while ν'' is the frequency corresponding to ν at the redshift along the photon path. The cross-sections for ionization are calculated using the fits of Verner et al. (1996).

Finally, the total rate of energy deposition per unit volume is

$$\epsilon_{\rm X}(\boldsymbol{x},\ z) = \sum_i n_i\int_{\nu_{\rm th}}^\infty d\nu\sigma_i(\nu)J_{\rm X}(\boldsymbol{x},\ z,\ \nu)\left(h\nu - h\nu_{\rm th}^i\right), \quad (22)$$

where $i = $ H I, He I, He II, n_i is the number density and $h\nu_{\rm th} = E_{\rm th}$ is the threshold energy for ionization. To get the total heating rate, we multiply this by the fraction of energy converted into heat $f_{\rm heat}$, obtained using the fitting formulae of Shull & van Steenberg (1985). We then evolve the gas temperature using

$$\frac{dT_K}{dt} = \frac{2T_K}{3n}\frac{dn}{dt} + \frac{2\epsilon_{\rm X} f_{\rm heat}}{3k_B n}, \quad (23)$$

where n is the proper number density of all particles. In order to evolve this equation through our simulation box, we set the initial condition for the gas temperature at $z = 24.9$ to be $T_K = 14.43$ K. The latter temperature is derived by assuming the adiabatic cooling of the gas since recombination for our fiducial cosmological model. In setting this initial condition we also assume that the gas is homogeneously cooled to this temperature at $z = 24.9$. Note that this is the same initial temperature as in our constant-temperature case where we ignore fluctuations in X-ray heating of gas, among others.

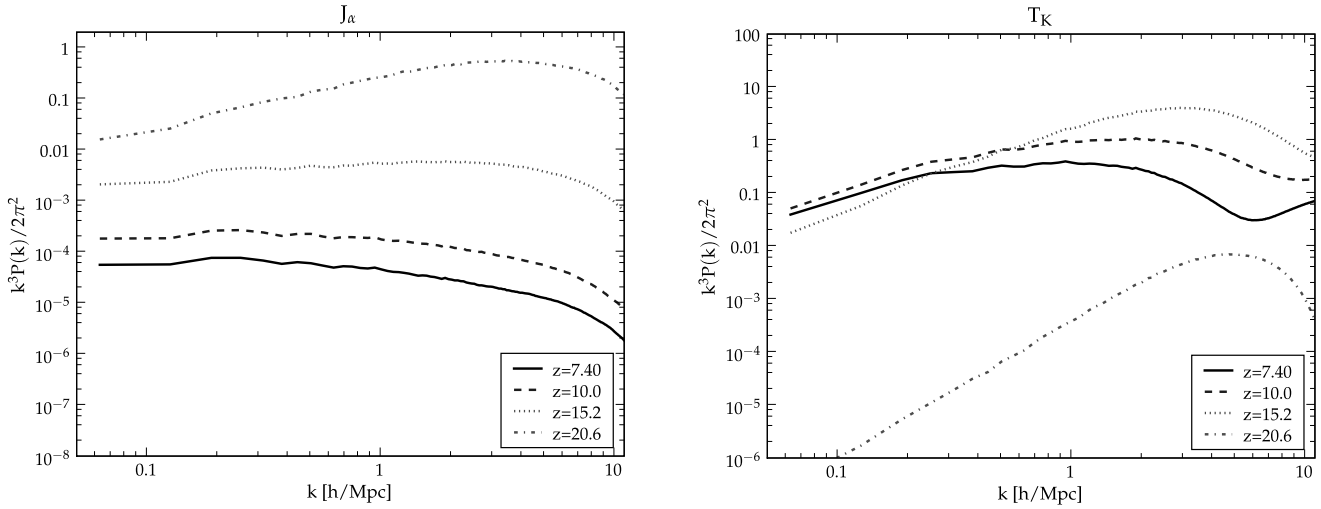

FIG. 5.—*Left*: Power spectra of the Lyα flux at several redshifts divided by the square of the mean flux. *Right*: Power spectra of the gas temperature due to X-rays divided by the average squared at each redshift. [*See the electronic edition of the Journal for a color version of this figure.*]

As $f_{\rm heat}$ depends on the free electron fraction in the IGM, x_e, we must also evolve x_e using

$$\frac{dx_e}{dt} = \epsilon_{\rm X} \frac{f_{\rm ion}}{nE_{\rm th}}, \tag{24}$$

where $f_{\rm ion}$ is the fraction of energy converted into ionizations which also depends on x_e (note that $\epsilon_{\rm X}$ also depends on x_e through n_i in eq. [22]). Note that this term is quite important since otherwise we get $x_e \sim 0$ and $f_{\rm heat} \sim 0$ in the IGM from UV ionization while $f_{\rm heat} \sim 0.01$–0.1 when $x_e \sim 10^{-8}$ to 10^{-4} instead of 0. We neglect primary ionizations from X-rays, since secondary ionizations dominate at large radii from halos and UV ionizations dominate at small radii. In making the above calculation, since $f_{\rm heat} \propto x_e^{1/4}$ (Shull & van Steenberg 1985), we approximate it by only considering the ionization of hydrogen and by setting $E_{\rm th} = 13.6$ eV. Both recombinations and corrections from helium are typically not important for calculating x_e, which stays small over the redshift range of interest. Figure 2 shows the evolution of x_e in the IGM for the simulation, which remains small at all times. Note that x_e is defined in the neutral IGM outside of fully ionized H II regions.

4. THE 21 cm SIGNAL: SIMULATIONS

In order to obtain the 21 cm brightness temperature from simulations, we basically need to apply equation (8). Both $f_{\rm H\,I}$ and ρ_b are already obtained by the simulation, as these properties are calculated with the evolution of the dark matter distribution. On the other hand, the spin temperature, T_S, is calculated at the postprocessing stage since the radiative transfer calculations of the initial run do not take into account the Lyα photons and X-ray heating. Usually it is assumed that $T_S \gg T_\gamma$ (e.g., the number density of hydrogen atoms in the triplet level is saturated), so that one does not need to worry about the spin temperature contribution to the 21 cm signal (Mellema et al. 2006). However, this assumption should only be safe for $z < 10$, so that one needs to consider the evolution of the spin temperature for a proper treatment of the 21 cm signal at the higher redshifts provided by this simulation. Moreover, fluctuations in the Lyα coupling and X-ray heating may be important at high redshifts (Barkana & Loeb 2005; Pritchard & Furlanetto 2007; Semelin et al. 2007). Therefore, we present here a full calculation of these fluctuations on the high-redshift signal probed by the simulation.

4.1. *Coupling Parameters*

Calculation of the collisional coupling parameter from equation (10) is straightforward. In this case we can easily include perturbations due to fluctuations in $n_{\rm H\,I}$ and n_e. In order to obtain the radiative coupling parameter, y_α we need to determine the comoving photon emissivity directly from the simulation using

$$\epsilon_\alpha(\boldsymbol{x},\ \nu,\ z) = {\rm SFRD}(\boldsymbol{x},\ z)\epsilon_b(\nu), \tag{25}$$

where SFRD($\boldsymbol{x}$, z) is again the star formation rate density from the simulation (in terms of the number of baryons in stars per comoving volume and proper time) and $\epsilon_b(\nu)$ is the spectral distribution function of the sources (defined as the number of photons per unit frequency emitted at ν per baryon in stars). Note that we are assuming that stars dominate over miniquasars for the radiative coupling. We consider separately the spectral distribution function from Pop II stars (Leitherer et al. 1999) and Pop III stars (Bromm et al. 2001; but see also Barkana & Loeb 2004). We then apply directly equation (13) to the simulation boxes. We can speed up this calculation by noting that the integral can be written in terms of a convolution between the SFRD and a specified kernel.

Figure 5 (*left*) shows the power spectrum of the J_α fluctuations from the simulation. The power spectrum is dominated by large-scale fluctuations at low redshifts, since most of the photons propagated through the entire box and fluctuations represents a small percentage of the overall Lyα photon flux. At large redshift (around $z \simeq 20$), most of the Lyα photons have not had time to propagate very far from halos and cluster around halos in 0.2–0.3 h^{-1} Mpc bubbles. However, these bubbles are highly clustered and have large bias factors related to the dark matter density field. The strong clustering of these small bubbles around first-light sources still leaves a Lyα intensity power spectrum that is strongly clustered even at high redshifts. Our measurement directly by postprocessing the star formation rate in our numerical simulation to extract properties of gas physics and 21 cm brightness temperature shows that there is no Poisson or shot-noise component in the Lyα intensity fluctuations. Analytical models that motivate detections of first-light galaxies from the 21 cm background have suggested a large shot noise for the Lyα intensity background fluctuations (Barkana & Loeb 2005), but we do not see such a component in our simulations to the extent that we can separate the Lyα intensity power spectrum at redshifts $z \sim 20$. While we

cannot comment on the appearance of shot noise even at higher redshifts or smaller scales, we hope in an upcoming paper to return to the general issue of detecting signatures of the highest redshifts galaxies in the 21 cm background by fully taking into account the instrumental systematics and foregrounds.

Finally, the Lyα coupling is determined through equation (11) (there will be extra fluctuations due to the S_α dependence on T_K and the matter density distribution). Analysis of the simulation shows that on average $y_\alpha > 1$ for $z \lesssim 17$ signaling the approach of the spin temperature to the gas temperature. Moreover, the Lyα coupling dominates over collisions up to $z \sim 22$ when $y_c \sim 10^{-2}$.

4.2. *Gas Temperature*

As described in § 2.1, the gas temperature provided by the simulation is essentially due to the virial temperature, given by the velocity dispersion of each particle. This effectively sets the gas temperature to $T \gtrsim 10^4$ K within the virial radius of halos. However, most of the heating is restricted to the high-density, ionized regions, while the neutral IGM continues to cool adiabatically. This means that most of the 21 cm signal would be seen in absorption even at the low redshifts when reionization is well underway.

X-ray heating, on the other hand, should heat the neutral IGM above the CMB temperature fairly easily and needs to be taken into account for a proper treatment of the 21 cm signal. We need therefore to include X-ray heating as part of our postprocessing to predict the spin temperature of gas and to calculate the brightness temperature of the 21 cm signal. Due to the clear separation between the ionized and neutral regions, we can consider the evolution of both heating mechanisms separately.

In order to calculate heating due to X-rays, we basically follow the procedure outlined in § 3.3, using the star formation rate density provided by the simulation. In order to use the same Fourier transform technique to speed up the temperature fluctuation calculation, we assumed the density of our species to be spatially constant and equal to the average in the computation of the optical depth. This approximation will reduce the optical depth around the halo, but as one gets farther away our optical depth should converge to the real one. We therefore probably underestimate the temperature in the halos and overestimate in the neighboring regions outside. For the spectral distribution function we assume $\alpha_S = 1.5$ (starbursts). Figure 5 (*right*) shows the dimensionless power spectrum of the gas temperature due to X-rays from the simulation. Note that these fluctuations are only relevant to the 21 cm signal as long as the gas temperature is not much higher than the CMB temperature. Thermal histories are also plotted in Figure 6 for $f_X = 0.1$, 1.0, and 10.0. These indicate that X-ray preheating can indeed heat the gas above the CMB temperature at the redshift range important for 21 cm observations, justifying the assumption that $T_S \gg T_{\rm CMB}$ at redshifts $z < 10$. Clearly, however, there is considerable uncertainty in what the exact thermal history is expected to be. Hereafter, when we calculate the 21 cm brightness temperature and its anisotropy, we assume $f_X = 1.0$. The analytical result we present here is also matched to the same X-ray intensity.

To highlight the reason why we consider X-ray heating as an inhomogeneous process, in Figure 7 we plot the volume filling factor of our simulation calculated by taking the ratio $\sum_i (4/3\pi\lambda^3)/V_{\rm simul}$, where λ is the mean free path around each X-ray source identified in the simulation with volume $V_{\rm simul}$. While photons with energies around 100 eV that are primarily responsible for heating propagate rapidly and fill the box by $z \sim 10$, the volume filling factor is below 1 around $z \sim 15$. This demonstrates that fluctuations in the heating of the gas by X-rays will be important around these redshifts.

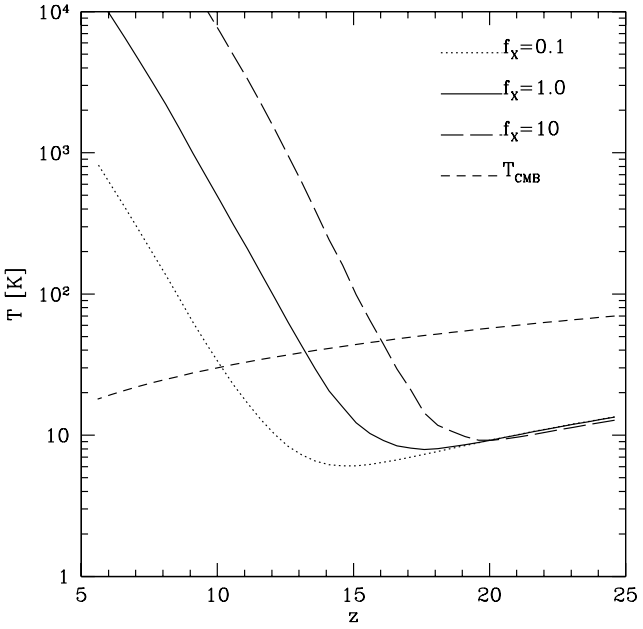

FIG. 6.—Evolution of gas temperature due to X-rays for several f_X (normalization of the X-ray luminosity).

4.3. *Brightness Temperature*

Finally, implementing equation (8), we can calculate the 21 cm brightness temperature for the simulation. Figure 8 shows the average evolution of this brightness temperature, together with the CMB temperature, gas temperature, and the spin temperature. Note that, as already pointed out, the spin temperature decouples from the CMB at $z \lesssim 17$ when $y_\alpha > 1$. The average 21 cm signal is clearly nonnegligible at high redshifts. Moreover the transition from emission to absorption depends on whether X-ray fluctuations are included. This is because regions with very low ionization fraction are still cold in spin temperature at low redshifts relative to the CMB and are therefore seen in absorption.

Figure 9 shows the evolution of the 21 cm signal with redshift for a set of k values. Again we can see that the signal strength actually increases for $z > 12$. The evolution of the 21 cm brightness fluctuations resemble strongly the average 21 cm brightness temperature. The fluctuations increase up to $z = 15$ as the coupling of the spin temperature to the gas temperature increases, then diminish during the absorption-emission transition down to $z = 11$, increasing or reaching a plateau in the $T_S \gg T_{\rm CMB}$, regime and then falling again at $z = 8$–9 when the ionization fraction reaches very high values and the universe fully reionizes.

The evolution of the power spectrum on large scales is qualitatively similar to that calculated in Pritchard & Loeb (2008), showing three peaks resulting from the periods where ionization, temperature, and Lyα fluctuations, respectively, come to dominate. We note that the dip at $x_i \sim 0.3$ occurs because on large scales the gas temperature is quite close to the CMB temperature at this redshift.

Figure 10 shows the brightness temperature for the same maps as in Figure 1, including fluctuations in the matter density, ionization fraction, Lyα coupling, and X-ray heating. Note that some of the features from the reionization maps are somewhat smeared in the brightness temperature maps due to the convolution with the density. At $z \sim 15$ perturbations in Lyα and X-ray heating are

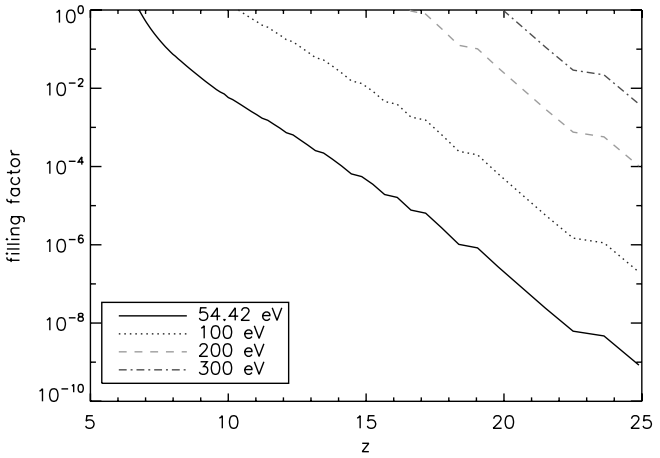

FIG. 7.— Volume filling factor of the X-ray radiation in the simulation as a function of redshift for several different values of the photon energy. While a photon with an energy such as 100 eV, which dominates X-ray heating, fills up the whole volume by $z \sim 10$ (i.e., the mean free path is larger than the simulation box length) at $z \sim 15$, the volume filling factor remains below 1 and X-ray heating at the onset of reionization is inhomogeneous. [*See the electronic edition of the Journal for a color version of this figure.*]

already nonnegligible and need to be properly taken into account when making 21 cm predictions.

Figure 11 (*top to bottom*) shows the 21 cm signal at $z = 20$, 15, and 10, whereby we separately include fluctuations in following quantities: matter density plus ionization fraction (*left*), matter density plus ionization fraction plus Lyα coupling (*middle*), and matter density plus ionization fraction plus X-ray heating (*right*). While at $z \sim 20$ fluctuations in the Lyα intensity field are important, at $z \sim 15$, features in the brightness temperature are sensitive to whether we model X-ray heating as an inhomogeneous source or whether we consider X-ray heating, wrongly, as uniform. This is the redshift in our simulation at which, due to X-ray heating, regions are beginning to be first detected in emission of the 21 cm brightness temperature instead of absorption as at higher redshifts.

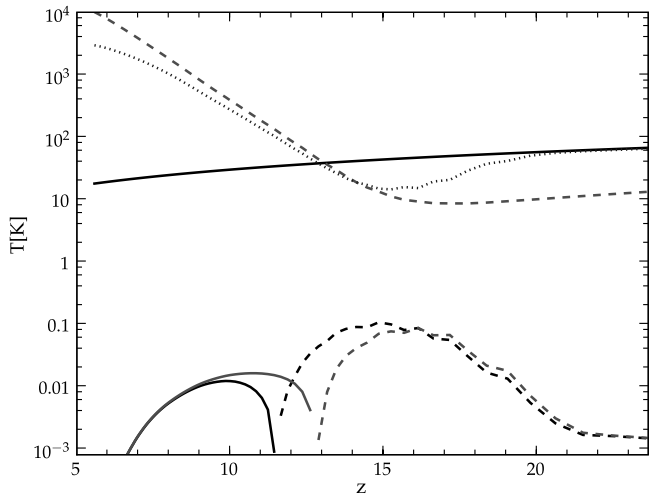

FIG. 8.— Temperature of the CMB (*solid line*), gas (*dashed line*), and spin (*dotted line*) as a function of z, in our simulation, in which we have included X-ray heating and collisional and radiative coupling. The bottom solid line shows the average brightness temperature when all fluctuations are taken into account, while the dashed one shows the absolute value (since it is negative at these redshifts). The lower gray line shows the brightness temperature when only fluctuations in the matter density and ionization fraction are included. [*See the electronic edition of the Journal for a color version of this figure.*]

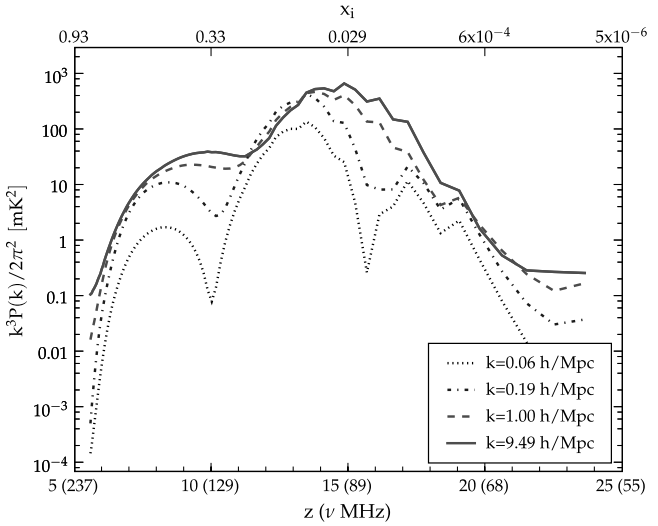

FIG. 9.— Evolution of the brightness temperature power spectrum with redshift. [*See the electronic edition of the Journal for a color version of this figure.*]

In terms of the inhomogeneous sources of the 21 cm brightness temperature, fluctuations in Lyα background makes the biggest difference at $z \sim 20$, as can be seen from the bottom middle panel. Here the locations with largest absorption signal in the 21 cm background is associated with first-light sources that have just formed first stars. A comparison of the middle panel of Figure 11 at $z = 20$ and the right panel at $z = 15$ shows that regions that are first dominating in emission due to X-ray heating at $z \sim 15$ are mostly the same regions that were first brighter in absorption at $z \sim 20$ due to Lyα coupling. At lower redshifts, however, during partial reionization, fluctuations in the brightness temperature are dominated by fluctuations in the ionization fraction modulated by the density field inhomogeneities. Thus, at the lower redshifts, $z < 10$, that will be targeted by the first-generation 21 cm interferometers, one can mostly ignore the effects associated with inhomogeneous X-ray heating or anisotropies in the Lyα coupling. This becomes clear in the next section when we compare the predictions related to the 21 cm brightness temperature anisotropy power spectrum with those related to analytical models.

5. OVERALL COMPARISON OF THE 21 cm SIGNAL: SIMULATION AND ANALYTICAL MODEL

Here we compare the power spectrum of the 21 cm signal from the simulation to a fast analytical power spectrum generator. The calculation of the analytical power spectra will basically follow the procedure outlined in Pritchard & Furlanetto (2007) using the model for the ionization fraction discussed in § 2.2, and we refer the reader to Pritchard & Furlanetto (2007) for further details.

When considering fluctuations in the 21 cm brightness temperature arising from variations in ionization and density, the correlation function of the brightness temperature can be expressed as

$$\xi_{T_b T_b} \equiv \left\langle \left(\delta T_b - \bar{\delta} T_b\right)\left(\delta T_b - \bar{\delta} T_b\right)\right\rangle = T_c^2 \left[\bar{f}_{\rm H\,I}^2 \xi_{\delta\delta} + \xi_{x_i x_i}(1 + \xi_{\delta\delta}) - \xi_{x_i\delta}\left(2\bar{f}_{\rm H\,I} - \xi_{x_i\delta}\right)\right], \quad (26)$$

and we use the procedure described in § 2.2 to calculate $\xi_{\delta\delta}$, $\xi_{x_i x_i}$, and $\xi_{x_i\delta}$. Note that we assume Gaussianity in this calculation but take into account the Gaussian terms from the four-point function (see the Appendix for a discussion of the effect of the non-Gaussian terms in eq. [26]). However, variations in the ionization fraction and density are not the only sources of 21 cm brightness temperature fluctuations, and we include anisotropies in X-ray

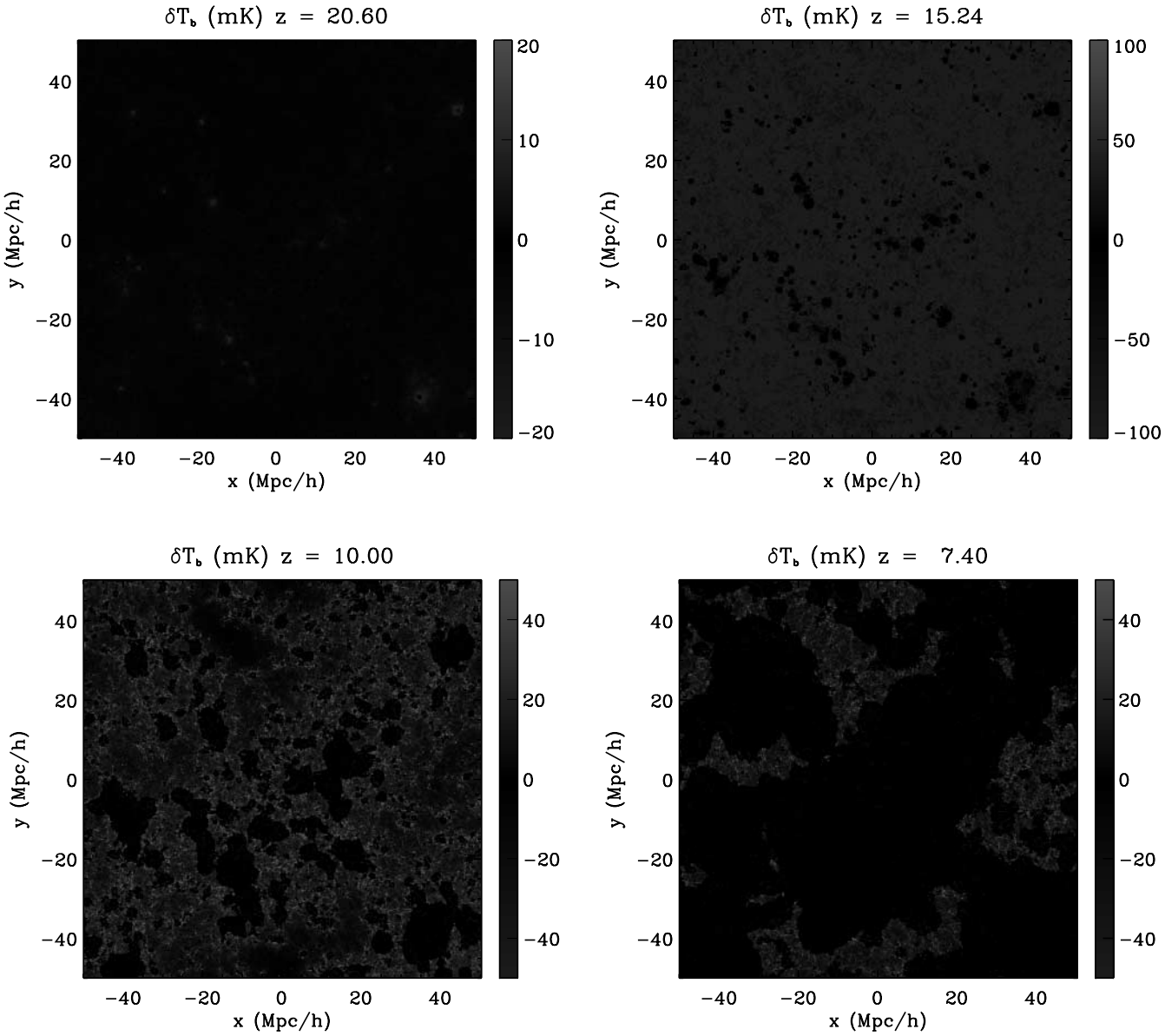

FIG. 10.—Maps of the 21 cm brightness temperature from the simulation, including all fluctuations, at redshifts $z = 20.6$, 15.2, 10.0, and 7.4, as labeled, corresponding to $\bar{x}_i = 0.0002$, 0.03, 0.35, and 0.84. [*See the electronic edition of the Journal for a color version of this figure.*]

heating and Lyα coupling separately (by following the procedure in Pritchard & Furlanetto 2007) so we can study how predictions change with whether one considers heating to be uniform, for example. We also follow the same procedure with the analytical calculation by adding various sources in step for easy comparison with numerical simulations.

In order to calculate the gas temperature (due to heating by X-rays), we need to obtain the analytical star formation rate and use it in equation (18). We model the star formation rate as tracking the collapse of matter, so that we may write the star formation rate per (comoving) unit volume:

$$\mathrm{SFRD} = \bar{\rho}_b^0(z) f_* \frac{d}{dt} f_{\mathrm{coll}}(z), \tag{27}$$

where $\bar{\rho}_b^0$ is the cosmic mean baryon density today. This formalism is appropriate for $z \gtrsim 10$, as at later times star formation as a result of mergers becomes important. For the analytical calculation, we do not distinguish between Pop II and Pop III stars and so use a value of $f_* = 0.1$, appropriate for Pop II stars, which dominate star formation at lower redshifts. While these parameters have not been fitted to the simulation data, the star formation rates from theory and simulation agree quite well. Fourier transforming the correlation function, $\xi_{T_b T_b}$, in equation (26) yields the desired power spectra. By first generating the correlation functions and then Fourier transforming we avoid having to consider the power spectrum convolution for the $\xi_{x_i x_i}\xi_{\delta\delta}$ and $\xi_{x_i\delta}\xi_{x_i\delta}$ terms.

In Figure 12 we show a comparison of the brightness temperature power spectrum between the analytical calculation and numerical simulations. Previously we have commented on the comparison between the analytical model prediction for the ionization fraction power spectrum (relative to the density field power spectrum) and the numerical simulation for the same quantity (Fig. 3 and § 2.2). We also expect the 21 cm prediction which uses only the ionization fluctuations and the density field as inhomogeneous sources to agree with the analytical calculation to the same extent that the two agreed previously. Thus, any differences

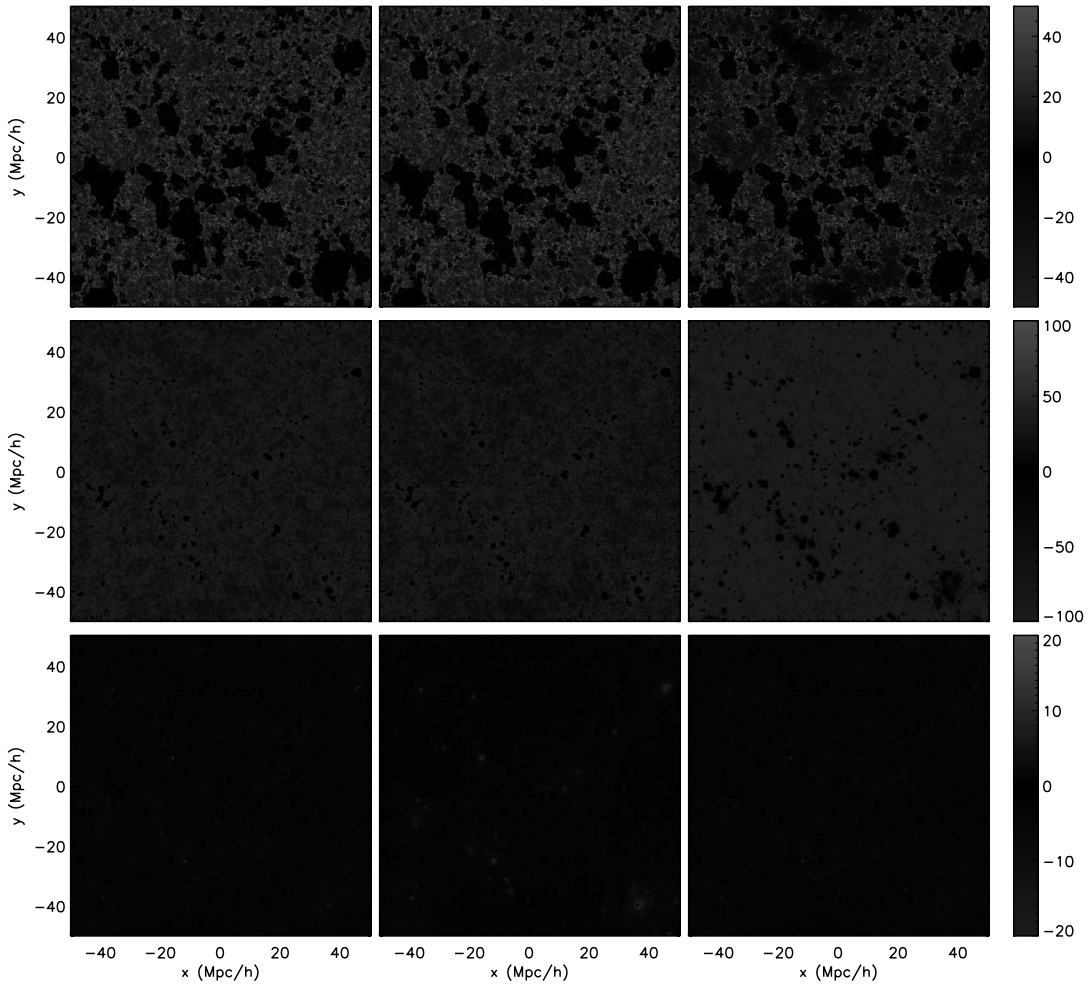

FIG. 11.—Maps of the 21 cm brightness temperature. *Top*: $z = 10$. *Middle*: $z = 15$. *Bottom*: $z = 20$. *Left*: Fluctuations in density and ionization fraction with homogeneous X-ray heating and Lyα radiation field. *Center*: Fluctuations in the Lyα background added, but homogeneous X-ray heating. *Right*: Fluctuations in X-ray heating, but uniform Lyα radiation field. [*See the electronic edition of the Journal for a color version of this figure.*]

beyond that of Figure 3 in Figure 12 between simulations and the analytical model are due to differences in the two prescriptions related to fluctuations in the Lyα intensity field and X-ray heating.

At low redshifts, we note that the two predictions agree very well to the extent that we can trust our simulations. At $z \sim 7$, the difference at $k \sim 0.1\ h\ \mathrm{Mpc}^{-1}$ is most likely to be that of the finite volume of the box and the cutoff associated with large-scale bubbles that have grown beyond the volume of the simulations, since we find less power in the simulation compared to that of the analytical model (see Fig. 3). At $z \sim 10$ the agreement between the simulation and analytical curves corresponding to density plus ionization fraction fluctuations (*dotted lines*) is very good. The difference in the solid lines is because X-ray perturbations are actually important at these redshifts. When we include fluctuations in X-rays, the very large, neutral scales ($k < 0.4$) are still "cold" at $z = 10$ (close to the CMB temperature) so we get a reduction in the 21 cm perturbations (this can also be seen in Fig. 9). The differences between the two prescriptions become more obvious at $z \sim 15$ and higher. At these high redshifts, as we have already noted, different sources of fluctuations make different contributions to the 21 cm brightness temperature fluctuations.

At $z \sim 15$, analytical calculations suggest a characteristic scale for 21 cm brightness temperature fluctuations with a shot-noise–like power spectrum at $k >$ a few $h\ \mathrm{Mpc}^{-1}$. This 21 cm power spectrum is dominated by fluctuations in the X-ray heating background, as can be established from a comparison between the dotted and dashed lines related to the analytical calculation at $z \sim 15$. At this redshift, the analytic model shows a considerable deficit of power on small scales when compared to the simulation and inhomogeneous X-ray heating is included. This appears to be a result of the analytic model assuming a tight cross-correlation between temperature and density fluctuations on all scales. Since the $P_{T\delta}$ term contributes with negative sign during the absorption epoch, P_{21} is reduced. It appears, however, that on small scales the cross-correlation between density and temperature is small. On large scales, the negative sign of the density-Lyα cross-correlation can be seen where the full calculation lies below that where Lyα fluctuations are ignored. If we set $P_{T\delta}$ to zero the analytic calculation gives much better agreement with the simulation on small scales. Clearly, improvements to the simple model of X-ray heating given in Pritchard & Furlanetto (2007) are necessary to resolve this problem. Note also that the dashed line is slightly higher than the total contribution shown by the solid line due to the anti-correlation between X-rays and Lyα fluctuations.

At $z \sim 20$, fluctuations in the X-ray heating are not the dominant source of 21 cm brightness temperature fluctuations, which is instead a combination of density perturbations and Lyα coupling.

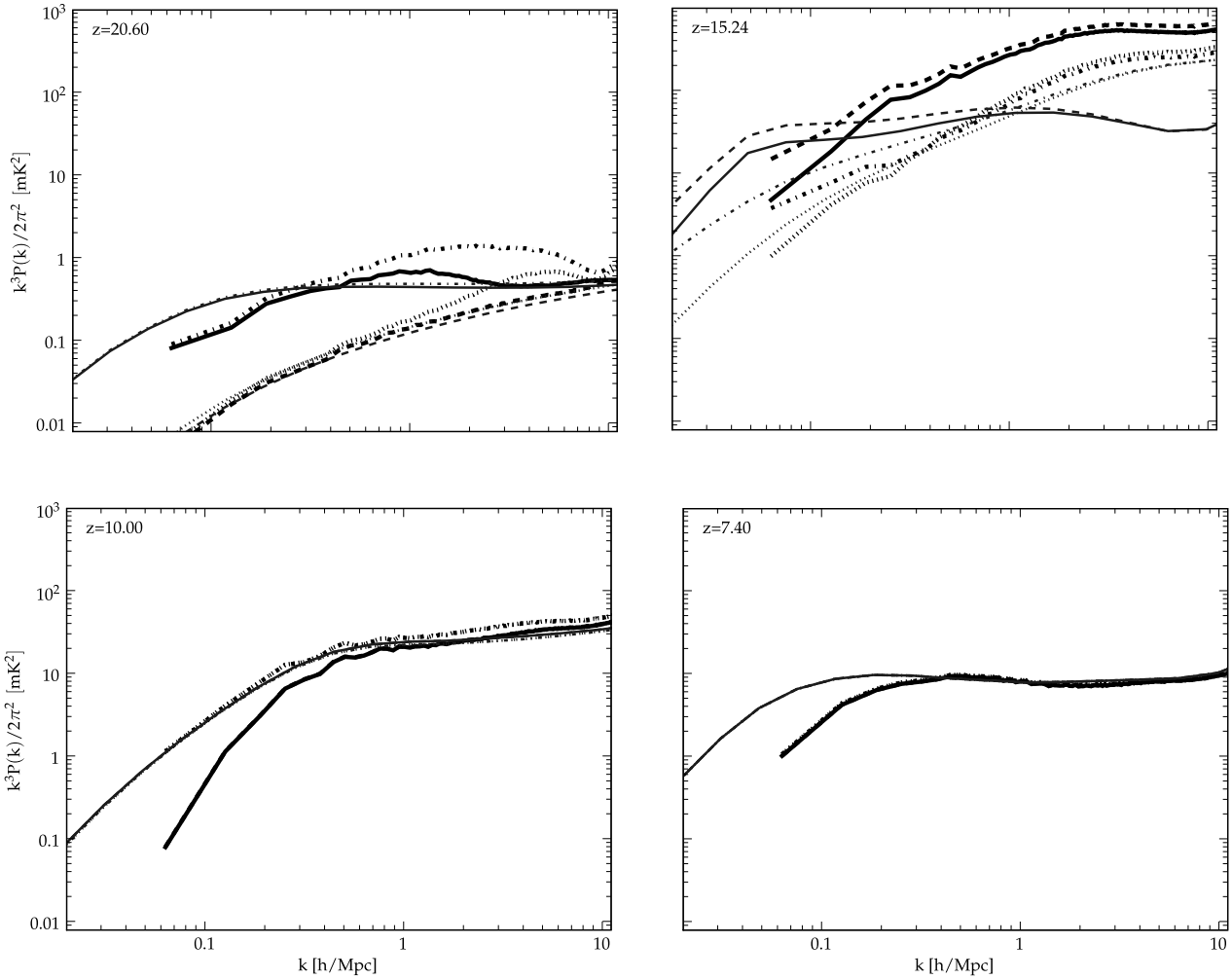

FIG. 12.—Power spectra of the 21 cm brightness temperature for the simulation (*thick curves*) vs. theory (*thin curves*). *Solid lines*: All fluctuations included; *dotted lines*: fluctuations in the matter density (ρ_m) plus ionization fraction (x_i); *dot-dashed lines*: fluctuations in ρ_m plus x_i plus Lyα; *dashed lines*: perturbations in ρ_m plus x_i plus X-rays. [*See the electronic edition of the Journal for a color version of this figure.*]

While there are general differences at $z \gtrsim 10$ between the analytical model and our numerical simulation, we note that these still lead to predictions that agree within a factor of a few, while at $z < 10$, the agreement is better than 30% and at $z \sim 7$ it is significantly better over the wavenumber range where we can make a comparison. Given that simple fitting formulae can be written down to model the ionization fraction power spectrum, which we outlined in § 2.2, it is likely that one can quickly calculate the 21 cm power spectrum at low redshifts as a function of the density field power spectrum. For reasons that we have previously discussed to enable quick exploration of the parameter space of 21 cm experiments, we suggest that analytical calculations, complemented by well-calibrated fitting formulae, can be trusted. For parameter estimation with data from upcoming interferometers, it may be necessary to improve beyond the fitting functions, however.

We note that comparisons such as the one we have performed between an analytical model and a numerical simulation of reionization, which was postprocessed to extract properties of the 21 cm brightness temperature, have been performed in the literature and that they draw conclusions similar to ours, i.e., that analytical calculations are adequate for parameter predictions and measurements with 21 cm data (Zahn et al. 2007). Our work differs from these previous comparisons in that for the first time, as far as we know, we extend the comparisons to redshifts beyond 8 and comment on the agreement even out to $z \sim 20$. To do this, we are forced to model fluctuations in X-ray heating and Lyα intensity field, since, as we have shown, these inhomogeneous sources make significant contributions to 21 cm brightness temperature fluctuations at $z \gtrsim 10$. At low redshifts, even after including fluctuations in Lyα coupling and X-ray heating, we find that the fluctuations in the 21 cm brightness temperature are dominated by fluctuations in the ionization fraction and the density field. Thus, previous analytical and numerical simulation comparisons, which only considered physics on ionization bubbles and their distribution in detail, remain valid.

6. SUMMARY AND CONCLUSIONS

Using a new large-volume, high-resolution simulation of cosmic reionization based on a hybrid code for N-body dark matter and radiative transfer of ionizing photons through an adaptive algorithm, we have measured several properties of the reionization process. We have focused our discussion on the low-frequency 21 cm signal associated with the neutral hydrogen distribution, which is now being pursued by a variety of interferometers as a probe of the reionization history of the universe.

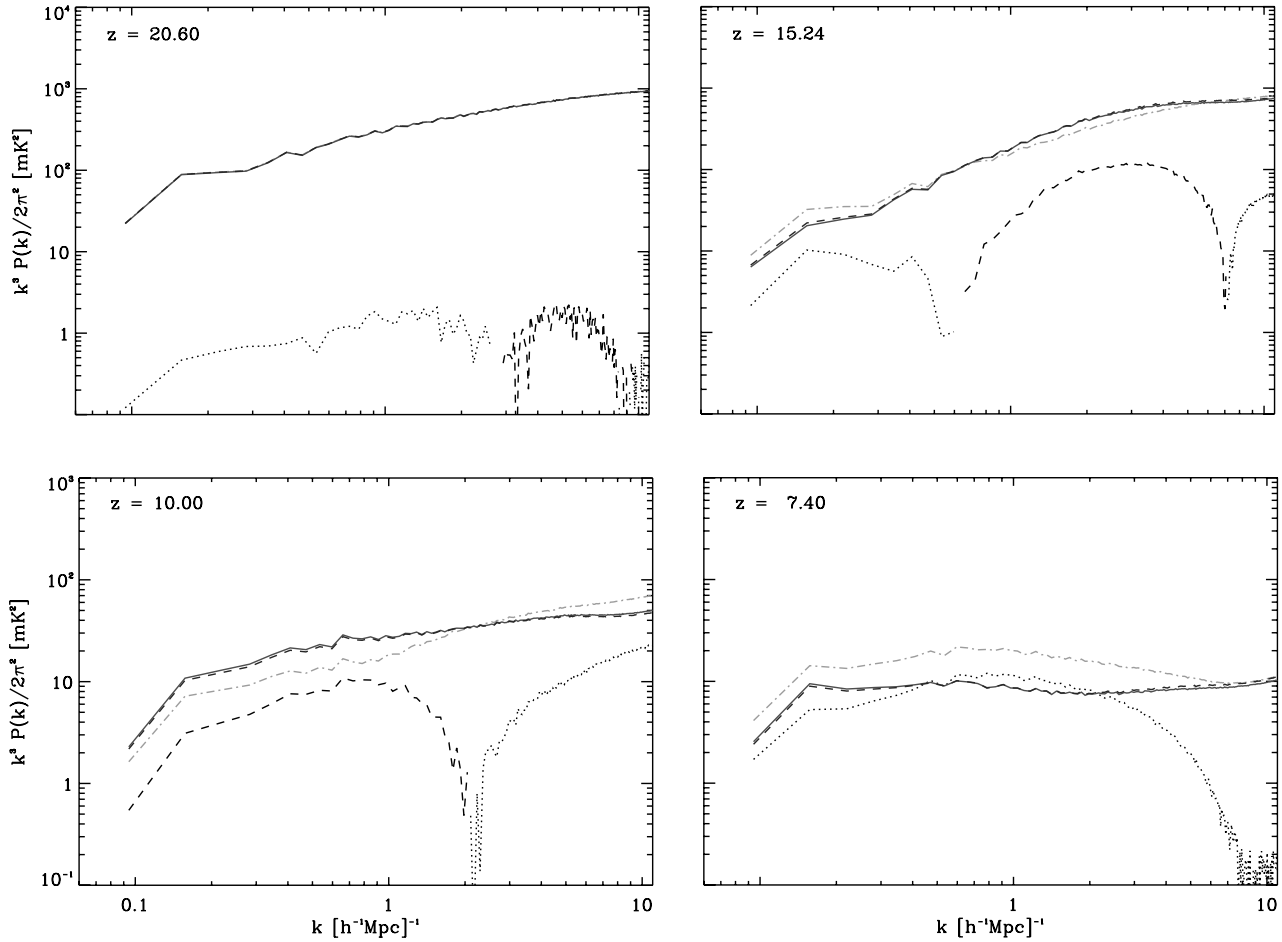

FIG. 13.—Three-dimensional power spectra of the brightness temperature and the contribution from the low- and higher order terms, when only considering fluctuations in the density and ionization fraction. The solid curves correspond to the power spectrum obtained directly from the simulation, while the dashed curves show the result of applying eq. (A1), which gives similar results to those expected. The dot-dashed lines show the contribution from the low-order terms. The dotted lines show the negative values of the higher order terms, while the lower dashed line shows the positive contribution from the higher order terms. [*See the electronic edition of the Journal for a color version of this figure.*]

In this paper we have studied the extent to which statistical results from an analytical model are consistent with results extracted from the simulation. Note that first-principle simulations cannot be considered for baryon physics and star formation, so that the brightness temperature of the simulation 21 cm signal is derived by postprocessing the simulation with certain results based on analytical prescriptions of the reionization process.

In detail, we have compared the spatial clustering of the neutral gas fraction, ionization fraction, and the associated 21 cm signal from the neutral hydrogen distribution. Our study extends to high redshifts where the contribution from spin temperature is nonnegligible and we take into account the heating of the gas by X-rays and the effect of Lyα and inhomogeneous collisional coupling when calculating the 21 cm radio signal. We find very good agreement between simulations and an analytical model at low redshifts, although there are nonnegligible differences at higher redshifts ($z \gtrsim 10$) arising from differences related to X-ray heating and fluctuations in the Lyα coupling. At the redshift range that will be probed by the first-generation 21 cm experiments ($z < 9$), we find that simple analytical models coupled with fitting functions associated with the ionization fraction power spectrum can easily reproduce the results from the numerical simulation. Therefore, at these redshifts, we find that there are no remaining issues regarding the use of an analytical model to explore the parameter space relevant for future 21 cm surveys, when using estimators based on the power spectrum alone. At higher redshifts, detailed comparisons, especially with regard to gas temperature and Lyα coupling, may be desirable in order to improve current analytical models.

This work was partially supported by FCT-Portugal under grant PTDC/FIS/66825/2006 and was supported at the University of California, Irvine, by NSF CAREER AST 06-45427 and by the National Aeronautics and Space Administration (NASA) through grant number 11242 from the Space Telescope Science Institute (STScI), which is operated by the Association of Universities for Research in Astronomy (AURA), Inc., under NASA contract NAS5-26555. This research is also supported in part by grants AST 04-07176 and NNG06GI09G. A. A. is supported in part by a McCue Fellowship. H. T. is supported in part by NASA grant LTSA-03-000-0090. M. G. S. was partially supported by FCT-Portugal under grant BPD/17068/2004/Y6F6. J. P. is supported by NASA through Hubble Fellowship grant HST-HF-01211.01-A, awarded by STScI.

APPENDIX A

When non-Gaussian terms become important, equation (26) is no longer valid and we need to take into account the full four-point and three-point function in the power spectrum calculation of the brightness temperature (see Lidz et al. 2007). The full power spectrum is then

$$P_{21}(k) = T_c^2[\bar{f}_{\rm H\,I}^2 P_{\delta,\delta}(k) + P_{x_i,x_i}(k) - 2\bar{f}_{\rm H\,I} P_{x_i,\delta}(k) + 2P_{x_i\delta,x_i}(k) - 2\bar{f}_{\rm H\,I} P_{x_i\delta,\delta}(k) + P_{x_i\delta,x_i\delta}(k)], \quad \text{(A1)}$$

where $P_{a,b}$ is just the power spectrum between the quantity a and b.

To see the difference, we show in Figure 13 the power spectrum of the brightness temperature obtained directly from the simulation (only considering fluctuations in the density and ionization fraction), compared to the one obtained by just using the first three terms in the equation above (the "low-order" terms).

Note that all the power spectra used are obtained directly from the simulation. We also plot the contribution from the higher order terms (second line in the equation) plus the result of considering the full expression, which, as expected, is similar to the actual 21 cm power spectrum measured from the simulation.

We can see that only at higher redshifts can the contribution of the "higher order" terms be safely neglected. In addition to accounting for some of the differences in the power spectrum, non-Gaussianity can also be an important source of information, especially at the height of the reionization process (i.e., about $\bar{x}_i \sim 0.5$), when the ionization structure becomes quite non-Gaussian.

REFERENCES

Aghanim, N., Desert, F. X., Puget, J. L., & Gispert, R. 1996, A&A, 311, 1
Allison, A. C., & Dalgarno, A. 1969, ApJ, 158, 423
Barkana, R. 2007, MNRAS, 376, 1784
Barkana, R., & Loeb, A. 2001, Phys. Rep., 349, 125
———. 2004, ApJ, 609, 474
———. 2005, ApJ, 626, 1
Becker, R. H., et al. 2001, AJ, 122, 2850
Bharadwaj, S., & Ali, S. S. 2005, MNRAS, 356, 1519
Bock, J., et al. 2008, preprint (arXiv:0805.4207v1)
Bromm, V., Kudritzki, R. P., & Loeb, A. 2001, ApJ, 552, 464
Cen, R. 2003, ApJ, 591, 12
Cen, R., & McDonald, P. 2002, ApJ, 570, 457
Chen, X., & Miralda-Escudé, J. 2004, ApJ, 602, 1
Chuzhoy, L., & Shapiro, P. R. 2007, ApJ, 655, 843
Ciardi, B., Ferrara, A., & White, S. D. M. 2003, MNRAS, 344, L7
Cooray, A. 2004, Phys. Rev. D, 70, 063509
Cooray, A., & Sheth, R. 2002, Phys. Rep., 372, 1
Dijkstra, M., Haiman, Z., & Loeb, A. 2004, ApJ, 613, 646
Dunkley, J., et al. 2008, preprint (arXiv:0803.0586)
Fan, X., Carilli, C. L., & Keating, B. 2006a, ARA&A, 44, 415
Fan, X., et al. 2001, AJ, 122, 2833
———. 2006b, AJ, 132, 117
Field, G. B. 1959, ApJ, 129, 525
Furlanetto, S. R. 2006, MNRAS, 371, 867
Furlanetto, S. R., & Furlanetto, M. R. 2007, MNRAS, 374, 547
Furlanetto, S. R., McQuinn, M., & Hernquist, L. 2006a, MNRAS, 365, 115
Furlanetto, S. R., & Oh, S. P. 2005, MNRAS, 363, 1031
Furlanetto, S. R., Oh, S. P., & Briggs, F. H. 2006b, Phys. Rep., 433, 181
Furlanetto, S. R., & Pritchard, J. R. 2006, MNRAS, 372, 1093
Furlanetto, S. R., Sokasian, A., & Hernquist, L. 2004a, MNRAS, 347, 187
Furlanetto, S. R., Zaldarriaga, M., & Hernquist, L. 2004b, ApJ, 613, 16
———. 2004c, ApJ, 613, 1
Gnedin, N. Y. 2000, ApJ, 535, 530
Gnedin, N. Y., & Shaver, P. A. 2004, ApJ, 608, 611
Gunn, J. E., & Peterson, B. A. 1965, ApJ, 142, 1633
Haiman, Z., & Holder, G. P. 2003, ApJ, 595, 1
Hirata, C. M. 2006, MNRAS, 367, 259
Hirata, C. M., & Sigurdson, K. 2007, MNRAS, 375, 1241
Holder, G. P., Haiman, Z., Kaplinghat, M., & Knox, L. 2003, ApJ, 595, 13
Iliev, I. T., Mellema, G., Pen, U.-L., Merz, H., Shapiro, P. R., & Alvarez, M. A. 2006, MNRAS, 369, 1625
Kaplinghat, M., Chu, M., Haiman, Z., Holder, G. P., Knox, L., & Skordis, C. 2003, ApJ, 583, 24
Knox, L., Scoccimarro, R., & Dodelson, S. 1998, Phys. Rev. Lett., 81, 2004
Kohler, K., Gnedin, N. Y., & Hamilton, A. J. S. 2007, ApJ, 657, 15
Komatsu, E., et al. 2008, preprint (arXiv:0803.0547)
Kuhlen, M., Madau, P., & Montgomery, R. 2006, ApJ, 637, L1
Leitherer, C., et al. 1999, ApJS, 123, 3
Lewis, A., & Challinor, A. 2007, Phys. Rev. D, 76, 083005
Lidz, A., Oh, S. P., & Furlanetto, S. R. 2006, ApJ, 639, L47
Lidz, A., Zahn, O., McQuinn, M., Zaldarriaga, M., Dutta, S., & Hernquist, L. 2007, ApJ, 659, 865
Loeb, A., & Zaldarriaga, M. 2004, Phys. Rev. Lett., 92, 211301
Madau, P., Meiksin, A., & Rees, M. J. 1997, ApJ, 475, 429
Mao, Y., Tegmark, M., McQuinn, M., Zaldarriaga, M., & Zahn, O. 2008, Phys. Rev. D, 78, 023529
McQuinn, M., Furlanetto, S. R., Hernquist, L., Zahn, O., & Zaldarriaga, M. 2005, ApJ, 630, 643
McQuinn, M., Lidz, A., Zahn, O., Dutta, S., Hernquist, L., & Zaldarriaga, M. 2007, MNRAS, 377, 1043
McQuinn, M., Zahn, O., Zaldarriaga, M., Hernquist, L., & Furlanetto, S. R. 2006, ApJ, 653, 815
Mellema, G., Iliev, I. T., Pen, U.-L., & Shapiro, P. R. 2006, MNRAS, 372, 679
Mesinger, A., & Furlanetto, S. 2007, ApJ, 669, 663
Morales, M. F., & Hewitt, J. 2004, ApJ, 615, 7
Mortonson, M. J., & Hu, W. 2008, ApJ, 672, 737
Nusser, A. 2005, MNRAS, 359, 183
Oh, S. P., Cooray, A., & Kamionkowski, M. 2003, MNRAS, 342, L20
Ostriker, J. P., & Vishniac, E. T. 1986, ApJ, 306, L51
Page, L., et al., 2007, ApJS, 170, 335
Pritchard, J. R., & Furlanetto, S. R. 2007, MNRAS, 376, 1680
Pritchard, J. R., & Loeb, A. 2008, preprint (arXiv:0802.2102)
Razoumov, A. O., Norman, M. L., Abel, T., & Scott, D. 2002, ApJ, 572, 695
Santos, M. G., & Cooray, A. 2006, Phys. Rev. D, 74, 083517
Santos, M. G., Cooray, A., Haiman, Z., Knox, L., & Ma, C. 2003, ApJ, 598, 756
Santos, M. G., Cooray, A., & Knox, L. 2005, ApJ, 625, 575
Schaerer, D. 2002, A&A, 382, 28
———. 2003, A&A, 397, 527
Semelin, B., Combes, F., & Baek, S. 2007, A&A, 474, 365
Sethi, S. K. 2005, MNRAS, 363, 818
Shin, M.-S., Trac, H., & Cen, R. 2008, ApJ, 681, 756
Shull, J. M., & van Steenberg, M. E. 1985, ApJ, 298, 268
Sokasian, A., Abel, T., Hernquist, L., & Springel, V. 2003, MNRAS, 344, 607
Spergel, D. N., et al. 2007, ApJS, 170, 377
Trac, H., & Cen, R. 2007, ApJ, 671, 1
Verner, D. A., Ferland, G. J., Korista, K. T., & Yakovlev, D. G. 1996, ApJ, 465, 487
Vishniac, E. T. 1987, ApJ, 322, 597
Wouthuysen, S. A. 1952, AJ, 57, 31
Wyithe, J. S. B., & Loeb, A. 2003, ApJ, 586, 693
Zahn, O., Lidz, A., McQuinn, M., Dutta, S., Hernquist, L., Zaldarriaga, M., & Furlanetto, S. R. 2007, ApJ, 654, 12
Zaldarriaga, M. 1997, Phys. Rev. D, 55, 1822
Zaldarriaga, M., Furlanetto, S. R., & Hernquist, L. 2004, ApJ, 608, 622
Zygelman, B. 2005, ApJ, 622, 1356